

1 **Joint characterization of heterogeneous conductivity fields and pumping well**  
2 **attributes through iterative ensemble smoother with a reduced-order modeling**  
3 **strategy for solute transport**

4  
5 Chuan-An Xia<sup>1</sup>, Jiayun Li<sup>2\*</sup>, Bill X. Hu<sup>3</sup>, Alberto Guadagnini<sup>4,5</sup>, Monica Riva<sup>4\*</sup>

6  
7 <sup>1</sup>Zijin School of Geology and Mining, Fuzhou University, Fuzhou, China

8 <sup>2</sup>Fujian Provincial Key Lab of Coastal Basin Environment, Fujian Polytechnic Normal  
9 University, Fuqing, China

10 <sup>3</sup>School of Water Conservancy & Environment, University of Jinan, Jinan, China

11 <sup>4</sup>Dipartimento di Ingegneria Civile e Ambientale, Politecnico di Milano, Milano, Italy

12 <sup>5</sup>Sonny Astani Department of Civil and Environmental Engineering, Viterbi School of  
13 Engineering, Los Angeles, California 90089-2531, USA

14  
15  
16  
17 Submitted to: *Hydrology and Earth System Sciences*

18  
19 Corresponding author: Jiayun Li; Monica Riva

20 Email: lijy@fpnu.edu.cn; monica.riva@polimi.it

21

22

### Abstract

23 We develop and test an efficient and accurate theoretical and computational  
24 framework to jointly estimate spatially variable hydraulic conductivity and identify  
25 unknown pumping well locations and rates in a two-dimensional confined aquifer.  
26 The approach (denoted as iES\_ROM) integrates an iterative Ensemble Smoother (iES)  
27 with a Reduced-Order Model (ROM) for solute transport taking place across an  
28 otherwise steady-state groundwater flow field. This offers a computationally efficient  
29 alternative to the Full System Model (iES\_FSM) upon addressing the high  
30 computational demands of ensemble-based data assimilation methods, which typically  
31 require large ensemble sizes to characterize uncertainties in (randomly) heterogeneous  
32 aquifers. Our iES\_ROM is constructed through proper orthogonal decomposition. It is  
33 then evaluated across a collection of 28 test cases exploring variations in model  
34 dimension, ensemble size, measurement noise, monitoring network, and statistical  
35 properties of the (underlying randomly heterogeneous) conductivity field. Our results  
36 support the ability of iES\_ROM to accurately estimate conductivity and identify  
37 pumping well attributes under diverse configurations, attaining a quality of  
38 performance similar to iES\_FSM. When using moderate ROM dimensions ( $n = 25-30$ )  
39 and ensemble size (i.e., 500-1000), the accuracy of iES\_ROM does not vary  
40 significantly while computational time is reduced by nearly an order of magnitude.  
41 Our approach thus provides a reliable and cost-effective tool for inverse modeling in  
42 groundwater systems with uncertain parameters.

43 Keywords: reduced-order model; proper orthogonal decomposition; iterative

44 ensemble smoother; pumping well identification; groundwater

45 **1. Introduction**

46       Assessment of groundwater flow and transport scenarios is typically plagued by  
47 uncertainties associated with model structure and parametrization. A major source of  
48 uncertainty often examined concerns the poorly constrained assessment of pollution  
49 sources. Our ability to identify spatial locations of these sources exerts significant  
50 influence on the design of contaminant monitoring, management, and remediation  
51 strategies. Contaminant release to an aquifer is characterized through the spatial  
52 location of sources, the temporal variability of release fluxes, and solute  
53 concentrations involved (Chen et al., 2018; Xu et al., 2018; Mo et al., 2019).  
54 Uncertainties linked to groundwater abstraction scheduling also play a critical role, as  
55 operational details of pumping wells are not always fully documented. For example,  
56 this might correspond to a scenario where such information is not disclosed to ensure  
57 privacy protection or uncertainties are induced by geocoding practices and/or  
58 measurement devices. Further to this, in some regions groundwater may be accessed  
59 through wells that are not officially registered or fully documented by industrial  
60 operators and/or local residents. Despite the relevance of these issues, only limited  
61 research has been devoted to the identification and quantification of pumping rates  
62 and spatial locations of such hidden wells.

63       In this broad context, we recall that a considerable body of research has focused  
64 on estimating key parameters (such as hydraulic conductivity) in groundwater flow  
65 and transport models through ensemble-based Data Assimilation (DA) techniques  
66 (Chen and Zhang, 2006; Tong et al., 2013; Chen and Oliver, 2013; Zhang et al., 2018;

67 Xia et al., 2018, 2024). These approaches aim at enhancing the accuracy of simulated  
68 system states (e.g., hydraulic heads and solute concentrations). While their capability  
69 to jointly estimate parameters and update system states has been broadly explored,  
70 their high computational cost still constitutes a persistent limitation to their practical  
71 routine use. This challenge primarily stems from the requirement for a large number  
72 of realizations to ensure statistical convergence of Monte Carlo (MC) simulations  
73 (e.g., Ballio and Guadagnini, 2004) in the forecast step of the DA process, and to  
74 achieve reliable parameter estimates in the analysis step. The computational burden  
75 becomes particularly significant when the selected model describing the system  
76 behavior (hereafter termed as Full System Model (FSM)) must be repeatedly executed  
77 for systems characterized by strong nonlinearities or requiring high (space-time)  
78 resolution of state variables and parameters.

79 To alleviate these computational constraints, recent studies explore the benefit of  
80 relying on surrogate (or reduced-order) models that approximate the behavior of the  
81 full system while maintaining sufficient accuracy for inverse modeling workflows and  
82 Uncertainty Quantification (UQ).

83 In this framework, efforts to mitigate computational limitations of  
84 (ensemble-based) DA methods primarily focus on the adoption of localization  
85 techniques (e.g., Xia et al., 2018, 2024; Luo and Bahkta, 2020) or surrogate modeling  
86 strategies (e.g., Zhang et al., 2018; Mo et al., 2019 and references therein). Main  
87 advantages associated with localization approaches are related to the observation that  
88 they (*i*) substantially reduce computational costs upon requiring only a limited

89 number of Monte Carlo realizations of the FSM, while maintaining acceptable  
90 accuracy of the assimilated results, and (ii) retain a physically-based and  
91 mathematically-tractable formulation. As a notable drawback of these approaches, we  
92 note that the value of the information associated with diverse measurements may be  
93 partially suppressed due to the use of distance- or correlation-based localization,  
94 which might constrain the strength of the spatial influence of observations. As a  
95 consequence, the ensuing (empirical/sample) probability density functions (PDFs) of  
96 model parameters and system states often display reduced accuracy and fail to fully  
97 capture the underlying uncertainty structure. To mitigate these limitations, an  
98 alternative line of research explores the use of surrogate models (SMs), which aim at  
99 emulating the response of the Full System Model with significantly reduced  
100 computational cost while preserving the salient physics of the system.

101 Surrogate models are rapidly emerging as a promising complement to FSMs for  
102 reducing computational burdens associated with the forecast steps of ensemble-based  
103 DA procedures. Among the various SM strategies, data-driven approaches based on  
104 machine learning (e.g., Ju et al., 2018) and deep learning (e.g., Mo et al., 2019) can be  
105 employed for emulating groundwater flow and transport processes taking place in  
106 heterogeneous media. For example, Ju et al. (2018) rely on Gaussian Process  
107 regression to describe relationships between the coefficients of a Karhunen-Loève  
108 (KL) expansion (employed to characterize a spatially heterogeneous hydraulic  
109 conductivity field) and (point-wise) simulated observations. This approach is shown  
110 to achieve approximately an order of magnitude reduction in computational time as

111 compared with the standard iterative Ensemble Smoother (iES). Otherwise, this gain  
112 in efficiency is associated with a reduced accuracy in simulated hydraulic heads,  
113 which in turn compromises the reliability of the estimated conductivity field. Mo et al.  
114 (2019) employ deep autoregressive neural networks as an FSM surrogate to  
115 reconstruct conductivity fields and identify contaminant source characteristics.  
116 However, their approach still requires a significant computational effort, as it heavily  
117 relies on a high number (about 1,500 in their exemplary setting) of MC realizations of  
118 the FSM for network training. While these studies show a clear potential of  
119 data-driven surrogates for accelerating DA workflows, they also highlight the need for  
120 a fundamental trade-off between computational efficiency and model accuracy, thus  
121 underscoring the potential value of alternative surrogate modeling strategies.

122 In contrast to data-driven models, that typically operate as black-box  
123 representations, projection-based Reduced-Order Models (ROMs) are physics-based  
124 (e.g., Razavi et al., 2012; Asher et al., 2015; Chen et al., 2017; Xia et al., 2020, 2025).  
125 ROMs are typically constructed upon projecting the governing equations and  
126 boundary conditions ~~of the~~ onto a lower-dimensional subspace spanned by a set of  
127 basis functions. The latter are commonly derived through, e.g., Proper Orthogonal  
128 Decomposition (POD) of multiple FSM solutions, referred to as *snapshots*. This  
129 procedure effectively reduces the dimensionality of the system state space. The  
130 random field representing the system state can then be expressed as a linear  
131 combination of the dominant eigenfunctions obtained from the Fredholm integral  
132 equation associated with the covariance matrix of the snapshots. Leading

133 eigenfunctions are then identified as the basis functions defining the reduced subspace.  
134 Substantial computational savings are then achieved upon resting on the solution of  
135 the ensuing low-dimensional linear system. When implemented in the context of  
136 numerical MC frameworks, the collection of ROM-generated solutions constitutes  
137 what is commonly referred to as a Reduced-Order Monte Carlo (ROMC) simulation  
138 framework.

139 Reduced-order modeling has received growing attention in the context of  
140 groundwater flow (Pasetto et al., 2011, 2013, 2014; Li et al., 2013a; Boyce et al., 2015;  
141 Stanko et al., 2016; Xia et al., 2020, 2025) and solute transport (Luo et al., 2012; Li et  
142 al., 2013b; Rizzo et al., 2018) scenarios. Its potential is evidenced across a wide range  
143 of hydrogeological configurations, including confined (e.g., Pasetto et al., 2011) and  
144 unconfined (e.g., Stanko et al., 2016) aquifer systems, homogeneous (e.g., Li et al.,  
145 2013a) and heterogeneous (e.g., Pasetto et al., 2013) media, as well as scenarios with  
146 (e.g., Xia et al., 2020) or without (e.g., Pasetto et al., 2014) pumping wells operating  
147 therein. Several studies further advance development of ROMC strategies for UQ in  
148 groundwater flow modeling. Pasetto et al. (2014) show that the accuracy of UQ  
149 results relying on ROMC in the presence of steady-state groundwater flow strongly  
150 depends on the quality and the number of snapshots, the latter directly influencing  
151 representativeness of the basis functions. To mitigate this limitation, Xia et al. (2020)  
152 propose deriving basis functions as the leading eigenvectors of (second-order)  
153 approximations of hydraulic head covariances. The latter are obtained upon solving  
154 the associated moment equations for steady-state groundwater flow (Zhang and Lu,

155 2002; Xia et al., 2019). Even as reduction of the dimensionality of the head space  
156 provides substantial computational savings, projection of the basis functions onto the  
157 ensuing (typically large) system matrix remains computationally intensive, thereby  
158 still constituting a limiting factor to efficiency gains. Xia et al. (2025) address this  
159 challenge by extending their approach to perform dimensionality reduction for both  
160 (spatially variable) transmissivity and hydraulic head fields in a steady-state  
161 groundwater flow setting and achieving additional computational savings while  
162 maintaining high accuracy. Despite these advancements, most existing ROM and  
163 ROMC approaches are still fraught with difficulties in efficiently capturing strongly  
164 nonlinear system dynamics and adapting to evolving state conditions, underscoring  
165 the need for more flexible and computationally efficient reduced-order frameworks.

166 With reference to solute transport, ROMs have been developed for both  
167 homogeneous (Luo et al., 2012) and heterogeneous (Li et al., 2013b; Rizzo et al.,  
168 2018) aquifer systems. Li et al. (2013a) further consider construction of ROMs to  
169 tackle density-dependent groundwater flow taking place across homogeneous and  
170 heterogeneous domains. Otherwise, studies explicitly focusing on the development of  
171 ROMC approaches for UQ of solute transport remain limited. Although conceptual  
172 insights can be drawn from ROMC studies addressing groundwater flow (e.g., Pasetto  
173 et al., 2014; Xia et al., 2020, 2025), influence of key factors (such as, e.g.,  
174 dimensionality of the reduced concentration space and strength of hydraulic  
175 conductivity heterogeneity) on accuracy and robustness of ROMC-based UQ still  
176 remains poorly characterized.

177 Building upon these works, the present study introduces a novel framework that  
178 integrates the iES with a ROM for solute transport (hereafter referred to as  
179 iES\_ROM). The ensuing framework enables one to efficiently quantify uncertainty  
180 and jointly estimate system parameters in groundwater-related modeling scenarios.  
181 The proposed method is then applied to simultaneously identify pumping rate and  
182 spatial location of (otherwise hidden) wells operating within the system, while  
183 providing estimates of the spatially heterogeneous hydraulic conductivity field under  
184 conditions of steady-state flow and transient solute transport. In the iES\_ROM  
185 framework, the steady-state flow field is evaluated through the FSM, whereas the  
186 transient solute transport is represented by a computationally efficient ROM. The  
187 required snapshots and associated POD are generated only once. These are  
188 subsequently employed throughout the entire DA process, thus avoiding repeated  
189 high-fidelity simulations. To ensure transparent benchmarking, the performance of  
190 iES\_ROM is systematically compared with that of a reference approach (termed  
191 iES\_FSM) which relies entirely on the FSM associated with synthetic scenarios.  
192 Comparative analyses are performed across a variety of synthetic scenarios,  
193 encompassing diverse ROM dimensions, ensemble sizes, measurement qualities and  
194 quantities, as well as distinct statistical descriptors of the initial conductivity ensemble  
195 and snapshot sizes.

196 The study is organized as follows. Section 2 introduces the theoretical  
197 background of groundwater flow and solute transport and details the integration of  
198 ROMC simulation within the iES framework. Section 3 describes the test cases

199 designed to evaluate the proposed approach. Section 4 illustrates and discusses the  
200 main results, and Section 5 summarizes the key findings.

## 201 **2. Theory background and methodology**

### 202 **2.1 Groundwater flow and solute transport**

203 We consider two-dimensional steady-state groundwater flow governed by:

$$204 \nabla \cdot [K(\mathbf{x}) \nabla h(\mathbf{x})] + q_s(\mathbf{x}) = 0 \quad (1)$$

205 where  $\mathbf{x} = [x_1, x_2]$  is a vector of spatial coordinates in domain  $\Omega^2$ ;  $h$  is hydraulic  
206 head;  $K$  is (isotropic) hydraulic conductivity; and  $q_s$  is a source/sink term. We  
207 conceptualize  $K$  as a spatially heterogeneous random field, associated with a given  
208 spatial correlation structure. The source/sink term in Equation (1) corresponds to a  
209 production well associated with an uncertain pumping rate and location in the domain.  
210 Propagation of uncertainty related to model parameters and/or forcing terms onto  
211 hydraulic heads and fluxes is typically assessed through numerical Monte Carlo (MC)  
212 simulations (see, e.g., Ballio and Guadagnini, 2004; Xia et al., 2020, 2024, and  
213 references therein).

214 We consider (non-reactive) solute transport evolving in  $\Omega^2$  to be described  
215 through:

$$216 \nabla \cdot [D \nabla c(\mathbf{x}, t)] - \nabla \cdot (\mathbf{q}(\mathbf{x}) c(\mathbf{x}, t)) + \frac{q_s(\mathbf{x})}{\theta} c_s(\mathbf{x}, t) = \frac{\partial c(\mathbf{x}, t)}{\partial t} \quad (2)$$

217 Here,  $t$  denotes time;  $c$  is solute concentration;  $D$  is the (isotropic) dispersion  
218 coefficient;  $\theta$  is effective porosity;  $c_s$  is solute concentration corresponding to  $q_s$ ;  
219 and  $\mathbf{q}(\mathbf{x}) = -(K(\mathbf{x})/\theta) \nabla h(\mathbf{x})$  is an effective velocity associated with solute  
220 transport.

221 Numerical methods (e.g., finite differences or finite elements) are commonly  
 222 employed to discretize Equations (1) and (2) that are then solved within a numerical  
 223 MC context. The probability distribution of state variables of interest (e.g., heads or  
 224 concentrations) is then evaluated at  $N$  nodes of an aptly designed numerical grid.  
 225 Consistent with Section 1, we refer to the model corresponding to the numerical  
 226 solution of the above equations as the Full System Model (FSM). When the domain is  
 227 characterized by a large spatial extent and/or one is interested in exploring the system  
 228 behavior across long temporal windows, performing numerical MC simulations  
 229 relying on FSM is associated with a heavy computational burden. To circumvent this  
 230 issue, we rely on the development and implementation of a Reduced-Order Model  
 231 (ROM) strategy for solute transport. We note that in this study we employ ROM  
 232 solely for solute transport because only limited computational costs are associated  
 233 with the steady-state flow condition we consider, as opposed to simulating transport.  
 234 Hereafter, we refer to numerical MC analyses grounded on ROM as ROMC.

## 235 **2.2 Numerical Monte Carlo simulation framework for solute transport**

### 236 **2.2.1 Monte Carlo simulation setting for the Full System Model**

237 We rely on a standard finite element method to solve the FSM described in  
 238 Section 2.1. When considering a total simulation time  $T_s$ , we express the linear  
 239 system associated with the numerical solution of solute transport through FSM within  
 240 time interval  $[t, t + \Delta t]$  as:

$$241 \quad \mathbf{A}^i \mathbf{c}^i = \mathbf{F}^i \quad (3)$$

242 Here, superscript  $i$  refers the to the  $i^{\text{th}}$  MC realization ( $i = 1, \dots, N_{MC}$ ,  $N_{MC}$  being the

243 total number of MC simulations) of FSM;  $\mathbf{A}$  is the full-system stiffness matrix (of  
 244 size  $N \times N$ ), which embeds information on spatial velocity, dispersion, and effective  
 245 porosity;  $\mathbf{c}$  is the vector (of size  $N \times 1$ ) of solute concentration values; and  $\mathbf{F}$  is the  
 246 stress vector (of size  $N \times 1$ ) whose entries encompass source/sink terms and initial and  
 247 boundary conditions.

### 248 2.2.2 Reduced-order Monte Carlo simulation framework

249 We construct a reduced-order model for solute transport by approximating the  
 250 solution of solute concentration for the  $i^{\text{th}}$  MC realization of FSM. Consistent with the  
 251 work of Xue and Xie (2007) and Pinnau (2008), one can approximate  $\mathbf{c}^i$  as:

$$252 \quad \mathbf{c}^i \approx \sum_{j=1}^n \alpha_j^i \mathbf{p}_j = \mathbf{P} \boldsymbol{\alpha}^i \quad (4)$$

253 Here,  $\mathbf{P} = [\mathbf{p}_1, \mathbf{p}_2, \dots, \mathbf{p}_n]$  is a matrix (of size  $N \times n$ ,  $n$  being the dimension of the ROM)  
 254 collecting the  $n$  nodal basis functions that are here obtained through a Proper  
 255 Orthogonal Decomposition (POD) approach (see below);  $\boldsymbol{\alpha}^i = [\alpha_1^i, \alpha_2^i, \dots, \alpha_n^i]^T$  ( $T$   
 256 representing transpose) is a vector (of size  $n \times 1$ ) of Fourier coefficients (Pinnau, 2008).  
 257 Note that Equation (4) is different from a typical Karhunen-Loève expansion of  $\mathbf{c}^i$   
 258 (i.e.,  $\mathbf{c}^i \approx \langle \mathbf{c} \rangle + \sum_{j=1}^n \alpha_j^i \mathbf{p}_j = \langle \mathbf{c} \rangle + \mathbf{P} \boldsymbol{\alpha}^i$ , see Equation (11) in Li et al., 2013b). As we  
 259 illustrate in Section 2.3, relying on Equation (4) enables straightforward (i) coding  
 260 and (ii) compatibility with the iterative Ensemble Smoother (IES).

261 Substituting Equation (4) into Equation (3) and imposing the residual of the  
 262 model equation associated with the approximated solution to be orthogonal to the  
 263 projection space defined through  $\mathbf{P}$  yields:

$$264 \quad \mathbf{P}^T \mathbf{A}^i \mathbf{P} \boldsymbol{\alpha}^i \approx \mathbf{P}^T \mathbf{F}^i \quad (5)$$

265 Solving Equation (5) (which is a linear system of size  $n$ ) yields  $\alpha^i$  for the  $i^{\text{th}}$   
 266 MC realization of our ROMC strategy. Note that, when  $n \ll N$ , the computational  
 267 effort required by our ROMC is much less than that of the standard MC.

268 The basis functions forming the entries of  $\mathbf{P}$  are computed as the leading  
 269 eigenvectors (corresponding to the highest eigenvalues) of the covariance of solute  
 270 concentration evaluated through  $N_{sm}$  numerical solutions (i.e.,  $\mathbf{c}^1, \mathbf{c}^2, \dots$ , and  $\mathbf{c}^{N_{sm}}$ )  
 271 of the FSM. Here,  $N_{sm} = m \times N_t$ , where  $m$  is the number of MC realizations of  
 272 hydraulic conductivity that are randomly sampled from the initial ensemble of  $Y$   
 273 fields, each yielding  $N_t = T_s / \Delta t$  ( $\Delta t$  corresponding to a uniform time step)  
 274 numerical solutions of Equation (2). The leading eigenvectors are computed through  
 275 the Singular Value Decomposition (SVD) approach, i.e.:

$$276 \quad \mathbf{U}\mathbf{\Lambda}\mathbf{U}^T = \text{svd}(\mathbf{E}\mathbf{E}^T) \quad (6)$$

277 where  $\mathbf{E} = 1/\sqrt{N_{sm}} [\mathbf{c}^1, \mathbf{c}^2, \dots, \mathbf{c}^{N_{sm}}]$ ;  $\mathbf{U}$  (of size  $N \times N$ ) is the left singular matrix  
 278 whose  $j^{\text{th}}$  column is the  $j^{\text{th}}$  eigenvector of matrix  $\mathbf{E}\mathbf{E}^T$  corresponding to the  $j^{\text{th}}$  singular  
 279 value,  $\lambda_j$ ; and  $\mathbf{\Lambda} = \text{diag}([\lambda_1, \lambda_2, \dots, \lambda_N])$  whose entries are ranked in descending  
 280 order.

### 281 2.3 Iterative ensemble smoother

282 We denote by  $\mathbf{m} = [Y_1, Y_2, \dots, Y_N, \ln q_s, x_{1,q_s}, x_{2,q_s}]^T$  the vector (of size  $P = N+3$ )  
 283 whose entries correspond to the uncertain model parameters (i.e., the log-conductivity,  
 284  $Y = \ln K$ , field) and flow rate and location of a pumping well. The pumping rate is  
 285 parameterized in logarithmic form to ensure consistent scaling with the  
 286 log-conductivity field and to reduce disparities in parameter magnitudes. Such a

Formatted: Font color: Auto

Field Code Changed

Formatted: Font color: Auto

287 transformation is consistent with common practice in inverse modeling to improve  
 288 numerical conditioning, enhance stability of the estimation process, and mitigate  
 289 potential bias arising from large disparities in parameter magnitudes. We denote by  
 290  $\mathbf{m} = [Y_1, Y_2, \dots, Y_N, \ln q_s, x_{1,q_s}, x_{2,q_s}]^T$  the vector (of size  $P = N+3$ ) whose entries  
 291 correspond to the uncertain model parameters (i.e., the log conductivity,  $Y = \ln K$ , field)  
 292 and flow rate and location of a pumping well. In case the pumping rate and location  
 293 are known, then  $\mathbf{m} = [Y_1, Y_2, \dots, Y_N]^T$  and  $P = N$ . We further denote by  
 294  $\mathbf{d} = [d_1, d_2, \dots, d_O]^T$  the vector (of size  $O$ ) of the randomly perturbed observations  
 295 (i.e., measured head and concentration values). To estimate  $\mathbf{m}$ , we implement the iES  
 296 (Luo and Bhakta, 2020; Xia et al., 2024):

$$297 \begin{cases} \mathbf{m}^{k+1} = \mathbf{m}^k + \underline{\underline{\mathbf{K}}}_{Gain}^k \Delta \mathbf{d}^k \\ \underline{\underline{\mathbf{K}}}_{Gain}^k = \underline{\underline{\mathbf{S}}}_m^k (\underline{\underline{\mathbf{S}}}_d^k)^T \left( \underline{\underline{\mathbf{S}}}_d^k (\underline{\underline{\mathbf{S}}}_d^k)^T + \gamma^k \underline{\underline{\mathbf{C}}}_d \right)^{-1} \text{ with } \gamma^i = \xi^i \text{trace} \left( \underline{\underline{\mathbf{S}}}_d^i (\underline{\underline{\mathbf{S}}}_d^i)^T \right) / O. \\ \Delta \mathbf{d}^k = \mathbf{d} - g(\mathbf{m}^k) \end{cases} \quad (7)$$

298 Here, superscript  $k$  is the index of the iteration step; matrices  
 299  $\underline{\underline{\mathbf{S}}}_m^k = [\mathbf{m}_1^k - \bar{\mathbf{m}}^k, \dots, \mathbf{m}_{N_{MC}}^k - \bar{\mathbf{m}}^k] / \sqrt{N_{MC} - 1}$  (of size  $P \times N$ , where  $\bar{\mathbf{m}}^k = \sum_{j=1}^N \mathbf{m}_j^k / N_{MC}$ )  
 300 and  $\underline{\underline{\mathbf{S}}}_d^k = [g(\mathbf{m}_1^k) - g(\bar{\mathbf{m}}^k), \dots, g(\mathbf{m}_{N_{MC}}^k) - g(\bar{\mathbf{m}}^k)] / \sqrt{N_{MC} - 1}$  (of size  $O \times N$ , where  
 301  $g(\cdot)$  represents model operator being either FSM or ROM) collect the ensemble  
 302 anomalies of parameters and simulated observations associated with the  $k^{th}$  iteration  
 303 step;  $\underline{\underline{\mathbf{C}}}_d$  is the covariance matrix of observation errors;  $\mathbf{I}$  is the identity matrix (of  
 304 size  $O \times O$ ); and  $\xi^k$  is an adaptive coefficient (Luo et al., 2015) associated with each  
 305 iteration of the Levenberg-Marquardt (LM; Levenberg, 1944) algorithm. We set  $\xi^0$   
 306 = 10 in our showcase application examples (see Section 3) and follow Luo and

Formatted: Font color: Auto

Formatted: Font color: Auto

Formatted: Font: (Default) Times New Roman, 小四

Formatted: Font: (Default) Times New Roman, 小四

Field Code Changed

307 Bhakta (2020) to update its value for the remaining iteration steps.

308 In the case of  $g(\cdot)$  representing the model operator of ROM, we note that the  
309 approximation of solute concentration relying on Equation (4) is compatible with the  
310 implementation of Equation (7). The degree of compatibility of ROM to iES is  
311 reduced when considering a typical Karhunen-Loève expansion of  $\mathbf{c}^i$  (i.e.,  
312  $\mathbf{c}^i \approx \langle \mathbf{c} \rangle + \sum_{j=1}^n \alpha_j^i \mathbf{p}_j = \langle \mathbf{c} \rangle + \mathbf{P} \boldsymbol{\alpha}^i$ ). This is related to the observation that  $\langle \mathbf{c} \rangle$  evolves  
313 with time and needs to be evaluated at each time step. This, in turn, implies that  $m$   
314 numerical solutions of solute concentration through FSM need to be obtained to  
315 evaluate  $\langle \mathbf{c} \rangle$  at every outer iteration of iES. Hence, computational advantages of  
316 employing ROM are reduced while coding complexity increases. When  
317 approximating solute concentration via Equation (4), we only obtain  $m$  numerical  
318 solutions of solute concentration through FSM at the first outer iteration of iES.  
319 Leading eigenvectors are computed upon relying on these solutions and are then  
320 stored. The Fourier coefficients  $\boldsymbol{\alpha}^i$  associated with time interval  $[t, t + \Delta t]$  for each  
321 MC realization starting from the second outer iteration of iES are obtained solely  
322 through solving Equation (5).

323 If an outer iteration does not lead to reduction in data misfit, an inner iteration is  
324 triggered to progressively decrease the time step until a lower misfit is obtained.  
325 When implementing the LM optimization scheme, we set the maximum number of  
326 both inner and outer iteration to 10 (see also Luo and Bhakta, 2020).~~When~~  
327 ~~implementing the LM algorithm during optimization, we set both the inner and outer~~  
328 ~~iteration numbers equal to 10 (see also Luo and Bhakta, 2020).~~ Additionally, a

Formatted: Font color: Auto

329 stopping criterion  $(\delta_{k-1} - \delta_k) / \delta_{k-1} \times 100\% \leq 10^{-6}$  (where

330  $\delta_k = \frac{1}{N} \sum_{j=1}^N \left\{ \left( \mathbf{d}_j^k - g(\mathbf{m}_j^k) \right)^T \mathbf{C}_d^{-1} \left( \mathbf{d}_j^k - g(\mathbf{m}_j^k) \right) \right\}$ , is set.

## 331 2.4 Implementation and computational cost

332 We denote by iES\_FSM and iES\_ROM the approaches associated with coupling  
333 the iES with FSM and ROM, respectively. A workflow for iES\_ROM is depicted in  
334 Fig. 1. The total number of MC realizations is denoted as  $N_{MC}$ . Neglecting the  
335 computational cost of the inner iterations and assuming iES comprises  $N_{out}$  outer  
336 iterations, the main computational costs of either method can be divided into two  
337 components, corresponding to forecast and analysis step (Table 1), respectively. In the  
338 forecast step, a number of  $(N_{out} + 1)$  MC simulations for groundwater flow and solute  
339 transport are required. Otherwise, Equation (7) is evaluated  $N_{out}$  times in the  
340 analysis step. The steady-state groundwater flow is solved through the FSM in both  
341 iES\_FSM and iES\_ROM, with a computational cost of order  $O(N^3(N_{MC} + 1))$  for  
342 each forecast step. The main computational cost for the  $N_{MC}$  FSM-based MC  
343 realizations of solute transport at a single time step in iES\_FSM is  $O(N^3(N_{MC} + 1))$ ,  
344 while being  $O((sN + N^2)(N_{MC} + 1))$  (where  $s \approx 7$  or  $\approx 15$  in two and three  
345 dimensions, respectively) for iES\_ROM. These computational efforts correspond to  
346 the projection of the full-system stiffness matrix onto the reduced-order space of the  
347 system state (i.e., solute concentration). Computational costs associated with solving  
348 Equation (7) coincide for both approaches and are here denoted as  $C_8$ . We further note  
349 that, with reference to iES\_ROM, the  $N_{sn}$  solutions of solute concentration obtained  
350 through FSM (associated with a computational cost of order  $O(N^3 N_{sn})$ ) and the

Formatted: Font: (Default) Times New Roman, 小四

351 basis functions obtained through SVD (with a computational cost of order  $O(nN_{sn}^2)$ )  
352 are calculated only once and stored. When the grid mesh employed is large or the  
353 simulation time is long, computational savings through iES\_ROM compared with  
354 iES\_FSM become significant.

### 355 **3. Exemplary scenarios**

356 We consider a two-dimensional computational domain of size  $4 \times 2$  to simulate a  
357 synthetic sandbox-scale experiment where (non-reactive) solute transport under  
358 steady-state flow is considered (see Fig. 2). Here and hereafter, all quantities are given  
359 in consistent (length/mass/time) units. Concerning groundwater flow, the left and right  
360 sides of the domain are associated with constant head boundary conditions with  $H = 3$   
361 and 2, respectively. The top and bottom sides correspond to boundary conditions of no  
362 flow. A pumping well with an unknown pumping rate and location is considered in the  
363 setting. A fixed concentration boundary is set at point (0, 1) (see red triangle in Fig. 2)  
364 with a constant concentration of 100, while the initial concentration across the domain  
365 is set to zero. We use the standard finite element method to obtain the numerical  
366 solutions of head and concentration. The numerical mesh adopted comprises  $41 \times 21 =$   
367 861 nodes and 1,600 triangle elements. A uniform time step of 1 day is considered,  
368 our analyses encompassing a total simulation time of 10 days (i.e.,  $T_s = 10$  days and  $N_t$   
369  $= 10$ ).

370 The logarithm of conductivity ( $Y = \ln K$ ) is considered as a spatially  
371 heterogeneous (correlated) Gaussian random field with an exponential covariance  
372 function ( $C_Y$ ) given by:

373 
$$C_Y = \sigma_Y^2 \exp\left(-\left(\frac{d_{x_1}}{\lambda_{x_1}} + \frac{d_{x_2}}{\lambda_{x_2}}\right)\right) \quad (8)$$

374 where  $\sigma_Y^2$  is the variance of  $Y$ ;  $d_{x_i}$  ( $i = x, y$ ) is separation (lag) distance between  
 375 two given points in the  $i$ -direction;  $\lambda_{x_i}$  (with  $i = x, y$ ) is the correlation length of  $Y$  in  
 376 the  $i$ -direction. The corresponding mean of  $Y$  is denoted as  $\mu$ . The initial ensemble of  
 377  $Y$  fields is synthetically generated through the well-known and widely tested GSLIB  
 378 suite (Deutsch and Journel, 1998) upon setting  $\lambda_{x_1}$  and  $\lambda_{x_2}$  equal to 1.0 and 0.5,  
 379 respectively. The reference  $Y$  field (Fig. 1a) is generated upon setting  $\mu = 0.8$ ,  $\sigma_Y^2$   
 380  $= 1.0$ ,  $\lambda_{x_1} = 1.0$ , and  $\lambda_{x_2} = 0.5$ .

381 The pumping rate (i.e.,  $q_s$ ),  $x_1$  and  $x_2$  -coordinates (denoted as  $x_{1,q_s}$  and  
 382  $x_{2,q_s}$ , respectively) of the pumping location are considered to be random variables,  
 383 each associated by a Gaussian distribution. The gray zone in Fig. 2b encompasses the  
 384 possible locations where a pumping well is operating. The initial collection (ensemble)  
 385 of values of  $q_s$ ,  $x_{1,q_s}$ , and  $x_{2,q_s}$  and their reference counterparts are sampled from  
 386 Gaussian distributions characterized by mean (standard deviation) equal to 0.50 (0.25),  
 387 1.00 (0.25), and 1.00 (0.25), respectively. These settings ensure that the randomly  
 388 generated samples of  $x_{1,q_s}$  and  $x_{2,q_s}$  are mostly within the coordinate ranges  
 389 indicated by the gray zone in Fig. 2b. Reference values are  $q_s = 1.03$ ,  $x_{1,q_s} = 1.38$ ,  
 390 and  $x_{2,q_s} = 1.40$  (see Fig. 2b, red cross symbol). Figure 2c depicts the simulated head  
 391 field associated with the reference conductivity field, pumping rate, and location.  
 392 Figure 1d depicts simulated concentrations at the final simulation time. Observations,  
 393 including (steady-state) head and solute concentration at each time step, are collected

394 at a number (denoted as  $N_m$ ) of monitoring wells distributed across the aquifer  
395 according to some pre-defined patterns (Fig. 2b-d). Each measurement is taken as the  
396 sum of the simulated head (or concentration) and a white noise with zero mean and  
397 standard deviation equal to  $\sigma_{obs}$ .

398 To explore the potential of iES\_ROM, several showcases are designed to  
399 highlight key features of interest. Five groups of test cases (TCs) are designed and  
400 organized as detailed in the following (see also Table 1).

- 401 ➤ **Group A.** It includes twelve TCs (i.e., TC1-TC12), enabling us to compare  
402 performances of iES\_FSM and iES\_ROM associated with diverse values of  
403  $n$  when the pumping rate and locations are either known (TC1-TC6) or  
404 unknown (TC7-TC12). The dimension of the ROM is considered equal to  $\{5,$   
405  $10, 15, 20, 25, 30\}$ , these values being consistent with those most commonly  
406 analyzed in previous studies (Pasetto et al., 2014; Xia et al., 2020, 2025).
- 407 ➤ **Group B.** It includes four TCs (i.e., TC6 and TC13-TC15), enabling us to  
408 compare the performances of iES\_FSM and iES\_ROM with the largest  
409 value of  $n$  analyzed (i.e.,  $n = 30$ ) and considering diverse values of  $N_{MC}$   
410 corresponding to  $\{30, 100, 500, 10,000\}$ . The latter are values of  $N_{MC}$   
411 commonly tested in previous studies (Chen and Zhang, 2006; Xia et al.,  
412 2021, 2024).
- 413 ➤ **Group C.** It includes five TCs (i.e., TC6 and TC16-TC19), designed to  
414 analyze the ability of iES\_ROM to cope with diverse quality and quantity of  
415 available measurements. Performances of iES\_FSM and iES\_ROM are also

416 compared when  $\sigma_{obs} = \{0.001, 0.01, 0.1\}$  and the number of observation  
417 locations corresponds to a value selected from  $\{9$  (Fig. 2b),  $18$  (Fig. 2c),  $55$   
418 (Fig. 2d)}.

419 ➤ **Group D.** It includes five TCs (i.e., TC6 and TC<sub>20</sub>-TC<sub>23</sub>), enabling us to  
420 study the effect of  $\mu$  and  $\sigma_Y^2$  of the initial ensemble of  $Y$  on the  
421 accuracies of estimates of conductivity and pumping rate and well location  
422 through iES\_FSM and iES\_ROM. Values of  $\mu$  and  $\sigma_Y^2$  of the initial  
423 ensemble of  $Y$  fields are selected from  $\{-0.5, 1.2, 2.0\}$  and  $\{0.01, 1.0, 2.0\}$ ,  
424 respectively.

425 ➤ **Group E.** It includes six TCs (i.e., TC6 and TC<sub>24</sub>-TC<sub>28</sub>), with the aim of  
426 investigating the effect of  $N_{sn}$  on the accuracies of the estimation of  
427 conductivity and well pumping rate and location through iES\_ROM and on  
428 computation time requirements. Values of  $N_{sn}$  in TC<sub>24</sub>-TC<sub>28</sub> and TC6 are  
429 equal to 30, 100, 300, 500, 1,000, and 10,000, respectively.

430 Note that, without specified otherwise, default settings for the above mentioned  
431 TCs correspond to TC6 which is designed with  $n = 30$ ,  $N_{MC} = 10,000$ ,  $N_{sn} = 10,000$ ,  
432  $N_m = 55$ ,  $\sigma_{obs} = 0.01$ , and values of  $\mu$  and  $\sigma_Y^2$  of the initial ensemble of  $Y$  equal  
433 to 1.2 and 1.0, respectively. Except for TC<sub>8</sub>-TC<sub>12</sub>, the source/sink term is associated  
434 with uncertainty.

435 To quantify the accuracy of conductivity estimates through iES\_ROM and  
436 iES\_FSM, we consider absolute error between estimated and reference values of  $Y$   
437 (denoted as  $E_Y$ ) and estimate of the standard deviation (denoted as  $S_Y$ ) which are

438 defined as:

$$439 \quad E_Y = \frac{1}{N} \sum_{i=1}^N \left| \langle Y_i \rangle^{est} - Y_i^{ref} \right|; \quad S_Y = \sqrt{\frac{1}{N} \sum_{i=1}^N (\sigma_{Y,i}^2)^{est}} \quad (9)$$

440 where  $\langle Y_i \rangle^{est}$ ,  $(\sigma_{Y,i}^2)^{est}$ , and  $Y_i^{ref}$  denote estimated (ensemble) mean and variance,  
441 and reference value of  $Y$  at the  $i^{th}$  cell of the numerical grid, respectively.

442 Absolute errors and estimates of the standard deviations of  $\ln q_s$ ,  $x_{1,q_s}$ , and  
443  $x_{2,q_s}$  are employed to quantify the accuracy of the estimate of the pumping rate and  
444 well location:

$$445 \quad E_{q_s} = \left| \langle \ln q_s \rangle^{est} - \ln q_s^{ref} \right|; \quad E_{x_1} = \left| \langle x_{1,q_s} \rangle^{est} - x_{1,q_s}^{ref} \right|; \quad E_{x_2} = \left| \langle x_{2,q_s} \rangle^{est} - x_{2,q_s}^{ref} \right| \quad (10)$$

446 where  $\langle \ln q_s \rangle^{est}$ ,  $\langle x_{1,q_s} \rangle^{est}$ , and  $\langle x_{2,q_s} \rangle^{est}$  indicate estimated (ensemble) mean values  
447 of  $\ln q_s$ ,  $x_{1,q_s}$ , and  $x_{2,q_s}$  respectively; and  $q_s^{ref}$ ,  $x_{1,q_s}^{ref}$ , and  $x_{2,q_s}^{ref}$  are the reference  
448 values of  $q_s$ ,  $x_{1,q_s}$ , and  $x_{2,q_s}$ , respectively. Estimates of the standard deviations of  
449  $\ln q_s$ ,  $x_{1,q_s}$ , and  $x_{2,q_s}$  are:

$$450 \quad S_{q_s} = \sqrt{(\sigma_{\ln q_s}^2)^{est}}; \quad S_{x_1} = \sqrt{(\sigma_{x_{1,q_s}}^2)^{est}}; \quad S_{x_2} = \sqrt{(\sigma_{x_{2,q_s}}^2)^{est}} \quad (11)$$

451 where  $(\sigma_{\ln q_s}^2)^{est}$ ,  $(\sigma_{x_{1,q_s}}^2)^{est}$ , and  $(\sigma_{x_{2,q_s}}^2)^{est}$  denote estimated (ensemble) variances of  
452  $\ln q_s$ ,  $x_{1,q_s}$ , and  $x_{2,q_s}$ , respectively.

453 As an additional metric, we then rely on the average absolute difference between  
454 available data and model results:

$$455 \quad E_{obs} = \frac{1}{O} \sum_{i=1}^O \left| \langle d_i \rangle^{up} - d_i^{ref} \right| \quad (12)$$

456 where  $\langle d_i \rangle^{up}$  and  $d_i^{ref}$  correspond to the (updated) result of the simulation process  
457 and its reference observed counterpart at the  $i^{th}$  sampled location, respectively.

458 **4. Results and discussion**

459 **4.1 Impact of the dimension of the reduced-order model (Group A)**

460 Figure 3 depicts  $E_Y$  (Fig. 3a),  $S_Y$  (Fig. 3b), and  $E_{obs}$  (Fig. 3c) versus the  
461 number of outer iterations for test cases (TCs) 1-6 obtained through iES\_ROM and  
462 iES\_FSM, when well pumping rate and location are uncertain. Note that results  
463 obtained through iES\_FSM are independent of  $n$  (and are identical among TCs 1-6)  
464 and are taken as references. Percentage differences (denoted as  $\Delta E_Y$ ) between the  
465 values of  $E_Y$  obtained through iES\_ROM and iES\_FSM are depicted in Fig. 3d.  
466 Corresponding results associated with percentage differences between values of  $S_Y$   
467 ( $\Delta S_Y$ ) and of  $E_{obs}$  ( $\Delta E_{obs}$ ) are depicted in Fig. 3e and 3f, respectively.

468 Values of  $E_Y$ ,  $S_Y$ , and  $E_{obs}$  obtained at the end of the iteration procedure  
469 through iES\_ROM generally decrease with  $n$ . When  $n = 25$  or  $30$ , the values of  $E_Y$   
470 and  $S_Y$  based on iES\_ROM tend to approach their counterparts obtained through  
471 iES\_FSM. The latter generally correspond to the lowest values across TCs 1-6. These  
472 findings are consistent with the observation (Xia et al., 2020; 2025) that accuracy of  
473 ROM for  $n = 30$  and FSM are very similar for solute transport. They are also in line  
474 with the results of Li et al. (2013b), who documented a high degree of correlation  
475 between simulated concentrations provided by their ROM and FSM for non-reactive  
476 transport.

477 Figure 4 depicts  $E_Y$  (Fig. 4a),  $S_Y$  (Fig. 4b), and  $E_{obs}$  (Fig. 4c) for TCs 7-12  
478 obtained through iES\_ROM and iES\_FSM when the well characteristics are  
479 deterministically known. Similar to above, results obtained through iES\_FSM are

480 identical among TCs 7-12 and are taken as reference. Values of  $\Delta E_Y$ ,  $\Delta S_Y$ , and  
481  $\Delta E_{obs}$  are depicted in Fig. 4d, 4e, and 4f, respectively.

482 Consistent with what one can observe in Fig. 3, values of  $E_Y$ ,  $S_Y$ , and  $E_{obs}$   
483 obtained at the end of the iteration procedure for TCs 7-12 through iES\_ROM  
484 generally decrease with  $n$ . Except for the cases where  $n = 5$  or 10 (corresponding to  
485 low solution accuracy of ROM), values of  $E_Y$ ,  $S_Y$ , and  $E_{obs}$  for TCs 9-12 based on  
486 either iES\_ROM or iES\_FSM are lower than their counterparts related to TCs 3-6.  
487 These results suggest that the accuracy of conductivity estimates is lower when  $q_s$  is  
488 uncertain compared to the case where  $q_s$  is deterministic.

489 Figure 5 depicts the values of  $E_{x_1}$  (Fig. 5a),  $E_{x_2}$  (Fig. 5b),  $E_{q_s}$  (Fig. 5c),  $S_{x_1}$   
490 (Fig. 5d),  $S_{x_2}$  (Fig. 5e), and  $S_{q_s}$  (Fig. 5f) versus the number of outer iterations for  
491 TCs 1-6 obtained through iES\_ROM and iES\_FSM. Values of  $E_{x_1}$ ,  $E_{x_2}$ , and  $E_{q_s}$   
492 obtained through iES\_ROM approach their iES\_FSM-based counterparts as  $n$   
493 increases. This is consistent with the observation that increasing  $n$  improves the  
494 accuracy of the ROM-based solution (see also Li et al., 2013b), therefore enhancing  
495 the accuracy of the identification of the well attributes.

496 Figure 6 depicts the estimated (ensemble)  $Y$  fields for TCs 1-6 obtained through  
497 iES\_ROM and iES\_FSM, together with their reference  $Y$  field. The white circle and  
498 cross symbols in Fig. 6 denote the estimated and reference locations of the pumping  
499 well, respectively. As  $n$  increases, the estimated  $Y$  field obtained through iES\_ROM  
500 (Fig. 6a-6f) approaches its iES\_FSM-based counterpart and the reference  $Y$  field (Fig.  
501 6h). The accuracy of the iES\_ROM-based estimate of the location of the pumping

502 well generally increases with  $n$ , consistent with the nature of the findings illustrated in  
503 Fig. 5. Figure 7 depicts the estimated (ensemble)  $Y$  variance fields for TCs 1-6 based  
504 on iES\_ROM and iES\_FSM. The white circle and cross symbols therein denote the  
505 identified and reference locations of the pumping well, respectively. These results  
506 show that the variance of  $Y$  is overestimated when  $n$  is small. This is related to the  
507 observation that small values of  $n$  correspond to large modeling errors (i.e., low  
508 solution accuracy) of ROM (as also seen in Li et al. (2013b) and Pasetto et al. (2017)).  
509 The latter, in turn, imprint the low accuracy of conductivity estimates (see Fig. 6a in  
510 the case of  $n = 5$ ) and yield overestimated values for the variance of  $Y$  (see Fig. 7a).

511 Figure 8 depicts the empirical probability density function (PDF) of  $x_{1,q_s}$ ,  $x_{2,q_s}$ ,  
512 and  $\ln q_s$  at the end of the iteration procedure for TCs 1, 2, 4, and 6 as obtained  
513 through iES\_ROM and iES\_FSM, together with their counterparts associated with  
514 initial guess (black solid) and reference values (black dashed). One can observe that  
515 large values of  $n$  yield high accuracy for  $x_{1,q_s}$  and  $x_{2,q_s}$  estimates, as visually  
516 indicated by the compact supports associated with the empirical PDFs of  $x_{1,q_s}$  (Fig.  
517 8a) and  $x_{2,q_s}$  (Fig. 8b). The accuracy of the estimate of  $q_s$  is already acceptable  
518 when  $n = 5$ .

519 As an additional element, we explore the way the choice of the value of  $n$   
520 impacts the local PDFs of hydraulic head and solute concentration. We do so upon  
521 considering the results associated with three reference points (i.e., I, II, and III in Fig.  
522 2d) that are aligned in the direction of the mean groundwater flow. Figure 9 depicts  
523 the (sample) PDFs of (hydraulic) head at these three selected locations (Figs. 9a-9c)

524 obtained through iES\_ROM and iES\_FSM at the end of the iteration procedure for  
525 TCs 1, 2, 4, and 6. Black solid lines included therein indicate reference head values.  
526 Note that the PDFs stemming from iES\_FSM peak at values very close to their  
527 reference counterparts. Hence, the corresponding empirical PDFs are considered as  
528 reference. The logarithm absolute difference ( $\Delta$ PDF, evaluated as the pointwise  
529 log-ratio of the densities and corresponding to a local measure of relative likelihood  
530 between two empirical PDFs) between the PDFs of the head at points I-III obtained  
531 through iES\_ROM based on diverse values of  $n$  and their counterpart based on  
532 iES\_FSM are also shown in Figs. 9d-9f, respectively. One can see that a large value of  
533  $n$  (e.g.,  $n = 30$  for TC6) corresponds to high accuracy of the PDF of head, as  
534 quantified through a low value of  $\Delta$ PDF. Although the head solution is obtained by  
535 solving FSM, the accuracy of the conductivity estimate is impacted by  $n$ . The latter,  
536 therefore, impacts the accuracy of heads. Fig. 10 depicts results related to solute  
537 concentration. As expected, the PDFs stemming from iES\_FSM peak at values very  
538 close to their reference counterparts also in this case. Consistent with Fig. 9, a large  
539 value of  $n$  (e.g., 30 for TC6) corresponds to high accuracy in the delineation of the  
540 PDF of solute concentration.

541 As a complement to these results, values of the Kullback-Leibler Divergence  
542 (KLD) between the (sample) PDFs of head at the three reference points at the last  
543 outer iteration obtained through iES\_FSM ( $h_{\text{FSM}}$ ) and iES\_ROM ( $h_{\text{ROM}}$ ) with  $n = 5$   
544 (TC1), 10 (TC2), 20 (TC4), and 30 (TC6) are listed in Table S1 (see supplementary  
545 information). We recall that values of  $\text{KLD}(h_{\text{ROM}}||h_{\text{FSM}})$  (or  $\text{KLD}(h_{\text{FSM}}||h_{\text{ROM}})$ )

546 quantify (in a global sense) information loss when using  $h_{\text{FSM}}$  ( $h_{\text{ROM}}$ ) to approximate  
547  $h_{\text{ROM}}$  ( $h_{\text{FSM}}$ ). Values of  $\text{KLD}(h_{\text{ROM}}||h_{\text{FSM}})$  generally increase with  $n$ . This indicates that  
548 the difference between PDFs of  $h_{\text{ROM}}$  and  $h_{\text{FSM}}$  decrease as  $n$  increases. While the  
549 highest values of  $\text{KLD}(h_{\text{FSM}}||h_{\text{ROM}})$  correspond to  $n = 5$ , no clear decreasing trends  
550 with increasing  $n$  are observed. Furthermore, the difference between  $\text{KLD}(h_{\text{ROM}}||h_{\text{FSM}})$   
551 and  $\text{KLD}(h_{\text{FSM}}||h_{\text{ROM}})$  generally decreases as  $n$  increases. This is related to the  
552 observation that the accuracy of ROM tends to increase as the dimension of the  
553 reduced-order model increase. Values of KLD between the empirical PDFs of solute  
554 concentrations at the three selected reference points at the last outer iteration obtained  
555 through iES\_FSM ( $c_{\text{FSM}}$ ) and iES\_ROM ( $c_{\text{ROM}}$ ) with  $n = 5$  (TC1), 10 (TC2), 20 (TC4),  
556 and 30 (TC6) are listed in Table S2 (see supplementary information).

#### 557 **4.2 Effect of the ensemble size (Group B)**

558 Figure 11 depicts iES\_ROM- and iES\_FSM-based values of  $E_Y$  (Fig. 11a),  $S_Y$   
559 (Fig. 11b), and  $E_{\text{obs}}$  (Fig. 11c) versus the number of outer iterations for TCs 6 and  
560 13-15. Values of  $E_Y$  and  $E_{\text{obs}}$  decrease as the ensemble size  $N_{MC}$  increases (while  
561 the value of  $S_Y$  increases) regardless of the approach employed. With reference to  
562 TC13, we note that when  $N_{MC} = 30$  the values of  $E_Y$  decrease during the course of  
563 the first outer iterations to then increase during the last outer iterations, values of  $S_Y$   
564 dropping rapidly during the iteration procedure, regardless of the approach employed.  
565 This phenomenon is typically linked to the occurrence of filter inbreeding caused by a  
566 limited ensemble size (Chen and Zhang, 2006; Xia et al., 2018; 2024). Values of  $E_Y$   
567 and  $S_Y$  for TCs 6 and 13-15 obtained through iES\_ROM are overall similar to those

568 associated with iES\_FSM. The iES\_ROM-based value of  $E_{obs}$  obtained at the end of  
569 the iteration procedure for a given TC is typically larger than its iES\_FSM-based  
570 counterpart. This is linked to the observation that the limited system dimension of  
571 ROM induces low accuracy of concentrations and (possibly) heads due to low  
572 accuracy of conductivity estimates, pumping rate, and well locations.

573 Figure 12 depicts the values of  $E_{x_1}$  (Fig. 12a),  $E_{x_2}$  (Fig. 12b),  $E_{q_s}$  (Fig. 12c),  
574  $S_{x_1}$  (Fig. 12d),  $S_{x_2}$  (Fig. 12e), and  $S_{q_s}$  (Fig. 12f) versus the number of outer  
575 iterations for TCs 6 and 13-15 obtained through iES\_ROM and iES\_FSM. When  
576 increasing  $N_{MC}$ , values of  $E_{x_1}$ ,  $E_{x_2}$ , and  $E_{q_s}$  obtained through either iES\_ROM or  
577 iES\_FSM do not show a clear trend. Values of  $S_{x_1}$ ,  $S_{x_2}$ , and  $S_{q_s}$  generally increase  
578 with  $N_{MC}$ , a result that is consistent with the findings encapsulated in Fig. 11b. Similar  
579 findings are also documented by Xu and Gómez-Hernández (2018, their Fig. 17), who  
580 show that, when considering joint identification of contaminant sources and hydraulic  
581 conductivities, the accuracy of estimates of key attributes characterizing contaminant  
582 sources does not necessarily improve after some time and as data assimilation  
583 progresses. We further note that jointly estimating conductivity and identifying  
584 source/sink term attributes (in terms of flow rate and location) is associated with a  
585 highly nonlinear optimization process. Hence, the accuracies of location and pumping  
586 rate estimation through iES\_FSM are not always higher than those stemming from  
587 iES\_ROM in terms of the values of the metrics employed (i.e.,  $E_{x_1}$ ,  $E_{x_2}$ , and  $E_{q_s}$ ).

588 Figures 13 depicts the estimated (ensemble mean)  $Y$  fields for TCs 6 and 13-15  
589 obtained through iES\_ROM and iES\_FSM. Figure 14 depicts the associated  $Y$

590 variance fields for TCs 6 and 13-15 obtained through iES\_ROM and iES\_FSM. The  
591 white (black) circle and cross symbols in Fig. 13 (or Fig. 14) represent the identified  
592 and the reference locations of the pumping well, respectively. Visual comparison of  
593 Fig. 13 and Fig. 6h suggests that the estimated  $Y$  fields rendered through an ensemble  
594 size  $N_{MC} = 100$  (i.e., TC14) obtained through iES\_ROM and iES\_FSM are the closest  
595 ones to the reference  $Y$  field. Nevertheless, jointly analyzing Figs. 11a, 13, and 14  
596 reveal that the estimated  $Y$  field corresponding to  $N_{MC} = 10,000$  (TC6) obtained  
597 through iES\_ROM is the one most closest to the reference  $Y$  field in terms of  $E_Y (=$   
598  $0.41)$ . Additionally, the identified and reference locations of the pumping well  
599 obtained through either iES\_ROM or iES\_FSM are close to each other, thus  
600 supporting the capability of both approaches to identify the well location.

#### 601 **4.3 Effect of quality and available number of observations (Group C)**

602 Table 2 lists values of  $E_Y$ ,  $S_Y$ ,  $E_{obs}$ ,  $E_{x_1}$ ,  $E_{x_2}$ ,  $E_{q_s}$ ,  $S_{x_1}$ ,  $S_{x_2}$ , and  $S_{q_s}$  at  
603 the end of iteration procedure for TC16 (characterized by  $\sigma_{obs} = 0.001$ ), TC6 ( $\sigma_{obs}$   
604  $= 0.01$ ), and TC17 ( $\sigma_{obs} = 0.1$ ) obtained through iES\_ROM and iES\_FSM. Values of  
605  $E_Y$ ,  $S_Y$ ,  $E_{obs}$ ,  $E_{x_1}$ , and  $E_{q_s}$  generally increase as the quality of observations  
606 deteriorates, i.e.,  $\sigma_{obs}$  increasing from 0.001 to 0.1. These results are also consistent  
607 with prior findings by Xia et al. (2018) according to which accuracy of conductivity  
608 estimates increases as the quality of observations improves. Values of  $E_{x_2}$  obtained  
609 through iES\_ROM and iES\_FSM do not monotonically decrease as  $\sigma_{obs}$  decreases.  
610 This is typically related to the strong nonlinear nature associated with the optimization  
611 process (see also Xu and Gómez-Hernández, 2018).

612 Figure 15 depicts iES\_ROM- and iES\_FSM-based values of  $E_Y$  (Fig. 15a),  $S_Y$   
613 (Fig. 15b), and  $E_{obs}$  (Fig. 15c) versus the number of outer iterations for TCs 6 and  
614 18-19. Values of  $E_Y$  (or  $S_Y$ ) for TCs 18 (where the number of monitoring wells is  
615  $N_m = 9$ ), 19 ( $N_m = 18$ ), and 6 ( $N_m = 55$ ) obtained through iES\_ROM are similar to  
616 their iES\_FSM-based counterparts and decrease as  $N_m$  increases. Values of  $E_{obs}$   
617 obtained through iES\_FSM decrease as  $N_m$  increases, while iES\_ROM-based  
618 results do not display a clear trend with  $N_m$ . This result may be attributed to the fact  
619 that, while increasing the number of monitoring wells enhances the amount of  
620 information available for estimating hydraulic conductivity, errors introduced through  
621 model reduction influence the evolution of the solute concentration mismatch between  
622 observations and simulations during the iterative calibration process.

623 Figure 16 depicts the values of  $E_{x_1}$  (Fig. 16a),  $E_{x_2}$  (Fig. 16b),  $E_{q_s}$  (Fig. 16c),  
624  $S_{x_1}$  (Fig. 16d),  $S_{x_2}$  (Fig. 16e), and  $S_{q_s}$  (Fig. 16f) versus the number of outer  
625 iterations for TCs 6 and 18-19 obtained through iES\_ROM and iES\_FSM. Values of  
626  $E_{x_1}$  ( $E_{x_2}$ ,  $E_{q_s}$ ,  $S_{x_1}$ ,  $S_{x_2}$ ,  $S_{q_s}$ , or  $S_Y$ ) for TCs 18 (for a number  $N_m = 9$  of  
627 monitoring wells), 19 ( $N_m = 18$ ), and 6 ( $N_m = 55$ ) obtained through either  
628 iES\_ROM or iES\_FSM decrease as  $N_m$  increases. Values of the same metric (i.e.,  
629  $E_{x_1}$ ,  $E_{x_2}$ ,  $E_{q_s}$ ,  $S_{x_1}$ ,  $S_{x_2}$ , or  $S_{q_s}$ ) obtained through iES\_ROM and iES\_FSM are  
630 overall close to each other.

631 Figure 17 depicts the empirical PDF of  $x_{1,q_s}$ ,  $x_{2,q_s}$ , and  $\ln q_s$  at the end of the  
632 iteration procedure for TCs 18, 19, and 6 obtained through iES\_ROM and iES\_FSM,  
633 together with their reference counterparts (black dashed lines). One can observe that

634 increasing  $N_m$  leads to improved accuracy of the identification of pumping well  
 635 attributes, as suggested by the reduced support and location of the peaks of the PDFs  
 636 of  $x_{1,q_s}$  (Fig. 17a),  $x_{2,q_s}$  (Fig. 17b), and  $\ln q_s$  (Fig. 17c) obtained through either  
 637 iES\_ROM or iES\_FSM and observed as  $N_m$  varies from 9 to 55. On the basis of  
 638 these results, it is hard to tell which approach provides higher accuracy of pumping  
 639 well identification, solely in terms of Fig. 17. To complement these findings, Table S3  
 640 (see supplementary information) lists the values of KLD between the empirical PDFs  
 641 of  $x_{1,q_s}$  ( $x_{2,q_s}$ , or  $\ln q_s$ ) obtained through iES\_FSM (denoted as  $p_{FSM}$ ) and  
 642 iES\_ROM (denoted as  $p_{ROM}$ ) with  $n = 30$ , considering  $N_m = 9$  (TC18), 18 (TC19), and  
 643 55 (TC6), respectively. Values of  $KLD(p_{jROM}||p_{jFSM})$  (with  $j = x_{1,q_s}$ ,  $x_{2,q_s}$ , and  $\ln q_s$ )  
 644 show an overall decreasing trend as  $N_m$  increase, while  $KLD(p_{jFSM}||p_{jROM})$   
 645 consistently decreases with  $N_m$ . These results are consistent with the observation that  
 646 increasing the number of monitoring wells improves the accuracy of conductivity  
 647 estimates (as also seen by Tong et al. (2010) and Xia et al. (2018)) as well as pumping  
 648 rate and well location through both approaches, thus, in turn, reducing discrepancies  
 649 between the corresponding PDFs.

#### 650 4.4 Effect of the mean and variance of the initial ensemble of $Y$ (Group D)

651 Table 3 lists the values of  $E_Y$ ,  $S_Y$ ,  $E_{obs}$ ,  $E_{x_1}$ ,  $E_{x_2}$ ,  $E_{q_s}$ ,  $S_{x_1}$ ,  $S_{x_2}$ , and  $S_{q_s}$   
 652 at the end of the iteration procedure for TCs 20 (characterized by a mean  $\mu = -0.5$  of  
 653 the initial ensemble of  $Y$ ), 6 ( $\mu = 1.2$ ), and 21 ( $\mu = 2.0$ ) obtained through  
 654 iES\_ROM and iES\_FSM. We recall that the mean value employed to generate the  
 655 reference  $Y$  field is equal to 0.8. When the discrepancy between  $\mu$  and the mean

656 value of the reference  $Y$  field increases, the error metrics employed display an overall  
657 increase,  $E_{x_1}$  and  $E_{q_s}$  constituting notable exceptions. This finding is consistent  
658 with the behavior documented by Xia et al. (2024) who considered two  
659 correlation-based localization approaches to assess conductivity estimation accuracy  
660 with respect to the mean of the initial ensemble of  $Y$ .

661 Table 4 lists the values of  $E_Y$ ,  $S_Y$ ,  $E_{obs}$ ,  $E_{x_1}$ ,  $E_{x_2}$ ,  $E_{q_s}$ ,  $S_{x_1}$ ,  $S_{x_2}$ , and  $S_{q_s}$   
662 at the end of the iteration procedure for TCs 22 (characterized by a variance  $\sigma_Y^2 =$   
663 0.01 of the initial ensemble of  $Y$ ), 6 ( $\sigma_Y^2 = 1.0$ ), and 23 ( $\sigma_Y^2 = 2.0$ ) obtained through  
664 iES\_ROM and iES\_FSM. We recall that the reference  $Y$  field is characterized by a  
665 unit variance. The values of  $E_Y$  and  $E_{x_2}$  obtained through both approaches increase  
666 as the discrepancy between  $\sigma_Y^2$  and the variance of the reference  $Y$  field increases.  
667 The values of  $E_{obs}$ ,  $E_{x_1}$ , and  $E_{q_s}$  obtained through both approaches generally  
668 increase with  $\sigma_Y^2$ . Similarly, values of metrics employed to quantify variability of the  
669 final ensemble of realizations (i.e.,  $S_Y$ ,  $S_{x_1}$ ,  $S_{x_2}$ , and  $S_{q_s}$ ) consistently increase  
670 with  $\sigma_Y^2$ .

671 A joint analysis of the results illustrated in Sections 4.1, 4.2, and 4.3 suggests  
672 that  $E_Y$  and  $S_Y$  provided by both approaches show a consistent behavior as a  
673 function of the key feature of interest. Otherwise, the response of the metrics  
674 associated with the pumping well attributes provided by both approaches reflects the  
675 enhanced nonlinearity of the associated optimization process. Additionally, the  
676 accuracy of the conductivity estimate possibly contributes more to the minimization  
677 of the objective function than that of pumping well identification. Additionally, the

678 values of the metrics in Sections 4.1, 4.2, and 4.3 provided by the two approaches are  
679 generally consistent with each other, thus supporting the representativeness of the  
680 iES\_ROM-based results.

#### 681 **4.5 Effect of the snapshot size (Group E)**

682 Table 5 lists percentage differences of the values of the performance metrics  
683 considered (i.e.,  $E_Y$ ,  $S_Y$ ,  $E_{obs}$ ,  $E_{x_1}$ ,  $E_{x_2}$ ,  $E_{q_s}$ ,  $S_{x_1}$ ,  $S_{x_2}$ , and  $S_{q_s}$ ) at the end of  
684 the iteration procedure for TCs 24-28 obtained through iES\_ROM, considering their  
685 counterparts through TC6 as references. These results show that the values of  $E_Y$   
686 and  $S_Y$  systematically decrease as  $N_{sn}$  increases from 30 to 1,000, while the other  
687 metrics display an overall decreasing pattern. This is related to the observation that a  
688 larger snapshot size corresponds to a higher accuracy of basis functions (Pasetto et al.,  
689 2014). Otherwise, it is worth noting that snapshots are evaluated only once throughout  
690 the entire data assimilation processes, thus resulting in a limited computational cost.

691 A single forward simulation for TC28 requires approximately 13 minutes of CPU  
692 time on the hardware platform used in this study (13th Gen Intel® Core™  
693 i7-13700K 3.40 GHz with 32 GB RAM). The total CPU time required to complete  
694 TC6 upon relying on iES\_FSM is 122 minutes, whereas the corresponding CPU time  
695 required to complete TC28 through iES\_ROM is 28 minutes, thus representing a  
696 speedup of approximately a factor of 9. Percentage differences associated with  $E_Y$   
697 and  $S_Y$  are equal to 0.50% and 0.21%, respectively, suggesting that the  
698 computational gain is achieved with negligible loss of accuracy. To further quantify  
699 the approximation error introduced by the ROM, we evaluate the residual mean

Field Code Changed

Formatted: Font color: Auto

Field Code Changed

Formatted: Font: Italic

700 square errors between the concentration field obtained from the first realization of the  
701 initial ensemble using the full-scale model and the corresponding ROM solutions with  
702 reduced dimensions  $n = 5, 10, 15, 20, 25,$  and  $30$ . The ensuing error values are  $0.8630,$   
703  $0.4156, 0.2699, 0.1909, 0.1312,$  and  $0.1336,$  respectively, demonstrating systematic  
704 error reduction as the reduced dimension increases. We further note that all of the  
705 associated coefficients of determination are higher than  $0.99$ . A CPU time of about  $13$   
706 minutes is required for running TC28 (using a processor 13th Gen Intel(R) Core(TM)  
707 i7-13700K 3.40 GHz with 32 GB RAM). The CPU time required to complete TC6  
708 upon relying on iES\_FSM ( $122$  minutes) is about  $9$  times the corresponding CPU time  
709 required to complete TC28 through iES\_ROM ( $28$  minutes), percentage differences  
710 associated with  $E_Y$  and  $S_Y$  being equal to  $0.50\%$  and  $0.21\%$ , respectively. CPU  
711 time savings can become more pronounced during data assimilation for a groundwater  
712 system of large size, due to the higher memory requirements of iES\_FSM for storing  
713 and computing large-dimensional vectors and matrices as compared to iES\_ROM.

714 Additionally, we emphasize that relying on realizations of  $Y$  associated with  
715 (spatial) statistics different from their theoretical counterparts linked to the initial  
716 ensemble of  $Y$  fields can contribute to deteriorate the quality of the selected snapshots.  
717 Low quality snapshots yield low quality basis functions and low accuracy of ROM  
718 outcomes (see our results in Section 4.1; Pasetto et al., 2014; Xia et al., 2020). These  
719 elements, in turn, contribute to deteriorate the accuracy of conductivity estimates and  
720 pumping well attributes. Additional studies should be devoted to assess the potential  
721 of techniques (including, e.g., greedy algorithms) that might contribute to increase the

722 quality of snapshots.

## 723 **5. Conclusions**

724 This study addresses joint estimation of (uncertain, spatially heterogeneous)  
725 hydraulic conductivities and attributes (location and flow rate) of a pumping well in a  
726 two-dimensional confined aquifer in the presence of (non-reactive) solute transport  
727 taking place across a steady-state flow field. Our analyses rest on an iterative  
728 Ensemble Smoother (iES) coupled with a Reduced-Order Model (ROM) for solute  
729 transport (the overall strategy being denoted as iES\_ROM). The ROM is constructed  
730 via Proper Orthogonal Decomposition (POD), using basis functions derived from the  
731 numerical solutions of the Full System Model (FSM) over the entire simulation period.  
732 The pumping well is characterized by its spatial coordinates  $(x_{1,q_s}, x_{2,q_s})$  and a  
733 constant pumping rate  $q_s$ . The ROM can achieve a solution accuracy similar to that  
734 of the FSM, while significantly reducing computational demands. Notably, as stated  
735 above, the basis functions are computed only once throughout the iES\_ROM iteration  
736 process, thus further enhancing efficiency. As a benchmark, the traditional iES  
737 approach relying on the FSM (termed iES\_FSM) is also implemented to estimate  
738 conductivity and identify well attributes.

739 To assess the performance and robustness of the proposed iES\_ROM approach,  
740 twenty-eight test cases (TCs 1-28) are designed and structured according to five  
741 categories (Groups A-E; Section 3), each targeting different influencing factors. These  
742 include the dimension of the reduced-order model ( $n$ ), ensemble size ( $N_{mc}$ ), standard  
743 deviation of the white noise representing measurement error ( $\sigma_{obs}$ ), number of

744 monitoring wells ( $N_m$ ), mean ( $\mu$ ) and variance ( $\sigma_y^2$ ) of the initial log-conductivity  
745 field, and snapshot size ( $N_{sn}$ ). The performance of iES\_ROM is systematically  
746 compared with that of iES\_FSM using nine evaluation metrics, encompassing the  
747 absolute error ( $E_y$ ; Equation (9)) and estimated standard deviation ( $S_y$ ; Equation (9))  
748 between estimated and reference values of  $Y$ ; the absolute errors and estimated  
749 standard deviations of the pumping well coordinates and rate (Equation (10)); and the  
750 average absolute difference between simulated and reference observations ( $E_{obs}$ ;  
751 Equation (12)).

752 Our work leads to the following major conclusions.

- 753 1. Both iES\_ROM and iES\_FSM yield accurate estimates of hydraulic  
754 conductivity distributions and identify the pumping well attributes across a  
755 wide range of tested conditions, including variations in model dimension,  
756 ensemble size, measurement noise, number of monitoring wells, and  
757 statistical properties of the initial ensemble.
- 758 2. The iES\_ROM approach achieves estimation accuracy similar to that of  
759 iES\_FSM when using a moderate reduced-order dimension ( $n = 25$  or  $30$ ).  
760 Otherwise, relying on a small dimension (e.g.,  $n = 5$ ) yields filter divergence  
761 due to unaccounted model errors. Increasing  $n$  effectively mitigates this  
762 issue and enhances the stability of the iES\_ROM performance.
- 763 3. When hydraulic conductivity and pumping well attributes are jointly  
764 estimated, both iES\_ROM and iES\_FSM exhibit a slight reduction in the  
765 accuracy of conductivity estimates compared to scenarios where only

766 conductivity is estimated. This trend is reflected in the values of  $E_Y$ ,  $S_Y$ ,  
767 and  $E_{obs}$  across TCs 1-12. Under such joint estimation, results in terms of  
768  $E_Y$ ,  $S_Y$ , and  $E_{obs}$  with respect to different influencing factors remain of  
769 acceptable quality for both iES\_ROM and iES\_FSM, consistent with the  
770 patterns observed in conductivity-only estimation. The behaviors of the  
771 remaining performance metrics are mutually consistent and within  
772 acceptable ranges, although somewhat less orderly.

773 4. Relying on the iES\_ROM approach yields an accuracy similar to that of  
774 iES\_FSM in estimating hydraulic conductivity and identifying pumping well  
775 attributes for both moderate ( $N_{sm} = 500$  or  $1,000$ ) and large ( $N_{sm} = 10,000$ )  
776 snapshotensemble sizes. This result supports its robustness with respect to  
777 snapshotensemble size selection.

778 5. In terms of computational efficiency, iES\_ROM yields substantial time  
779 savings compared to iES\_FSM. For instance, with  $N_{sm} = 500$  and  $n = 30$ ,  
780 the CPU times for iES\_ROM and iES\_FSM are approximately 28 and 122  
781 minutes, respectively (i.e., iES\_FSM requires a computation time that is  
782 about nine times longer while yielding similar estimation accuracy).

783 Additional elements of interest for future studies on coupling iES with ROM can  
784 include analyses of transient saturated/unsaturated flows (in conjunction with, e.g.,  
785 time-dependent pumping strategy), reactive transport processes, and  
786 density-dependent flow/transport scenarios. Future efforts should also address  
787 characterization of aquifer heterogeneity upon relying on the theoretical framework

788 associated with generalized sub-Gaussian random fields (Riva et al., 2015; Xia et al.,  
789 2024), which may aptly represent non-Gaussian features and statistical scaling of  
790 subsurface properties. When considering nonlinear systems, reliance on discrete  
791 matrix interpolation schemes (Negri et al., 2015; Bonomi et al., 2017) appears to be a  
792 promising strategy to further enhance the computational efficiency and robustness of  
793 ROM-based approaches. Additional elements of interest associated with future studies  
794 on coupling iES with ROM include the analysis of transient saturated/unsaturated  
795 flow, reactive transport, and density dependent flow/transport scenarios. When  
796 considering nonlinear systems, reliance on discrete matrix interpolation schemes  
797 (Negri et al., 2015; Bonomi et al., 2017) constitutes a promising approach to enhance  
798 computational advantages of ROM.

799       Moreover, the values of  $N_{MC}$  that one should consider in a field application are  
800 case-dependent. In this context, localization techniques can be embedded in DA  
801 processes, as these can reduce negative influences of spurious correlation on  
802 parameter estimate arising from reliance on small ensemble sizes.

803 *Author contributions.* All authors contributed to the preparation of the manuscript.

804 *Acknowledgments.* This work was supported by the National Nature Science  
805 Foundation of China (Grant No. 42002247; [42430712](#)), Nature Science Foundation of  
806 Fujian Province, China (Grant No. 2025J01529; 2025J08248), and Opening Fund of  
807 Key Laboratory of Geohazard Prevention of Hilly Mountains, Ministry of Natural  
808 Resources (FJKLGH2024K008). M.R. acknowledges funding from the National  
809 Recovery and Resilience Plan (NRRP), mission 4 component 2 investment 1.4 - call

810 for tender no. 3138 of 16 December 2021, rectified by decree no. 3175 of 18  
811 December 2021 of Italian Ministry of University and Research funded by the  
812 European Union - NextGenerationEU, project code CN\_00000033, concession decree  
813 no. 1034 of 17 June 2022 adopted by the Italian Ministry of University and Research,  
814 CUP D43C22001250001, project title “National Biodiversity Future Center - NBFC”.

#### 815 **References**

- 816 Asher, M.J., Croke, B.F.W., Jakeman, A.J., Peeters, L.J.M., 2015. A review of  
817 surrogate models and their application to groundwater modeling. *Water Resour.*  
818 *Res.* 51, 5957-5973.
- 819 Ballio, F., Guadagnini, A., 2004. Convergence assessment of numerical Monte Carlo  
820 simulations in groundwater hydrology. *Water Resour. Res.* 40, W04603.
- 821 Boyce, S.E., Nishikawa, T., Yeh, W.W.G., 2015. Reduced order modeling of the  
822 newton formulation of modflow to solve unconfined groundwater flow. *Adv.*  
823 *Water Resour.* 83, 250-262.
- 824 Bonomi, D., Manzoni, A., Quarteroni, A., 2017. A matrix DEIM technique for model  
825 reduction of nonlinear parametrized problems in cardiac mechanics. *Comput.*  
826 *Methods Appl. Mech. Eng.* 324, 300-326.
- 827 Chen, Y., Zhang, D., 2006. Data assimilation for transient flow in geologic formations  
828 via ensemble Kalman filter. *Adv Water Resour.*, 29(8): 1107-22.
- 829 Chen, Y., Oliver, D. S., 2013. Levenberg–Marquardt forms of the iterative ensemble  
830 smoother for efficient history matching and uncertainty quantification.  
831 *Computational Geosciences*, 17(4): 689-703.

832 Chen, Z., Jaime Gomez-Hernandez, J., Xu, T., Zanini, A., 2018. Joint identification of  
833 contaminant source and aquifer geometry in a sandbox experiment with the  
834 restart ensemble kalman filter. *J. Hydrol.* 564, 1074-1084.

835 Deutsch, C.V., Journel, A.G., 1998. *GSLIB: Geostatistical Software Library and*  
836 *User's Guide*, second ed. Oxford University Press, New York.

837 Evensen, G., 2009. *Data Assimilation: The Ensemble Kalman Filter. Data*  
838 *Assimilation: The Ensemble Kalman Filter.*

839 Ju, L., Zhang, J., Meng, L., et al. 2018. An adaptive Gaussian process-based iterative  
840 ensemble smoother for data assimilation. *Adv. Water Resour.*, 115: 125-35.

841 Li, X., Chen, X., Hu, B.X., Navon, I.M., 2013a. Model reduction of a coupled  
842 numerical model using proper orthogonal decomposition. *J. Hydrol.* 507,  
843 227-240.

844 Li, X., Hu, B. X., 2013b. Proper orthogonal decomposition reduced model for mass  
845 transport in heterogeneous media. *Stochastic Environmental Research and Risk*  
846 *Assessment*, 27(5): 1181-91.

847 Luo, Z., Li, H., Zhou, Y., et al. 2012. A reduced finite element formulation based on  
848 POD method for two-dimensional solute transport problems. *Journal of*  
849 *Mathematical Analysis and Applications*, 385(1): 371-83.

850 Luo, X., Bhakta, T., 2020. Automatic and adaptive localization for ensemble-based  
851 history matching. *Journal of Petroleum Science and Engineering*, 184: 106559.

852 Mo, S., Zabarar, N., Shi, X., et al. 2019. Deep Autoregressive Neural Networks for  
853 High-Dimensional Inverse Problems in Groundwater Contaminant Source

854 Identification. *Water Resour. Res.*, 55(5): 3856-81.

855 Negri, F., Manzoni, A., Amsallem, D., 2015. Efficient model reduction of  
856 parametrized systems by matrix discrete empirical interpolation. *J. Comput. Phys.*  
857 303, 431-454.

858 Pasetto, D., Guadagnini, A., Putti, M., 2011. POD-based Monte Carlo approach for  
859 the solution of regional scale groundwater flow driven by randomly distributed  
860 recharge. *Adv. Water Resour.*, 34(11): 1450-1463.  
861 DOI:10.1016/j.advwatres.2011.07.003

862 Pasetto, D., Putti, M., Yeh, W.W.G., 2013. A reduced-order model for groundwater  
863 flow equation with random hydraulic conductivity: Application to Monte Carlo  
864 methods. *Water Resour. Res.*, 49(6): 3215-3228. DOI:10.1002/wrcr.20136

865 Pasetto, D., Guadagnini, A., Putti, M., 2014. A reduced-order model for Monte Carlo  
866 simulations of stochastic groundwater flow. *Computational Geosciences*, 18(2):  
867 157-169. DOI:10.1007/s10596-013-9389-4

868 Pasetto, D., Ferronato, M., Putti, M., 2017. A reduced order model-based  
869 preconditioner for the efficient solution of transient diffusion equations.  
870 *International Journal for Numerical Methods in Engineering*, 109(8): 1159-1179.  
871 DOI:10.1002/nme.5320

872 Pinnau, R., 2008. *Model Reduction via Proper Orthogonal Decomposition* /Schilders,  
873 W. H. A., Van Der Vorst, H. A., Rommes, J. *Model Order Reduction: Theory,*  
874 *Research Aspects and Applications.* Berlin, Heidelberg; Springer Berlin  
875 Heidelberg. 95-109.

876 Razavi, S., Tolson, B.A., Burn, D.H., 2012. Review of surrogate modeling in water  
877 resources. *Water Resour. Res.* 48

878 [Riva, M., Neuman, S.P., Guadagnini, A., 2015. New scaling model for variables and](#)  
879 [increments with heavy-tailed distributions. \*Water Resour. Res.\* 51, 4623-4634.](#)

880 Rizzo, C., de Barros, F., Perotto, S., Oldani, L., Guadagnini, A., 2018. Adaptive POD  
881 model reduction for solute transport in heterogeneous porous media. *Computat.*  
882 *Geosci.* 22, 297-308.

883 Stanko, Z.P., Boyce, S.E., Yeh, W.W.-G., 2016. Nonlinear model reduction of  
884 unconfined groundwater flow using pod and deim. *Adv. Water Resour.* 97,  
885 130-143.

886 Tong, J., Hu, B. X., Yang, J., 2010. Using data assimilation method to calibrate a  
887 heterogeneous conductivity field conditioning on transient flow test data.  
888 *Stochastic Environmental Research and Risk Assessment*, 24(8): 1211-23.

889 Xia, C.-A., Luo, X., Hu, B.X., Riva, M., Guadagnini, A., 2021. Data assimilation with  
890 multiple types of observation boreholes via the ensemble Kalman filter  
891 embedded within stochastic moment equations. *Hydrol. Earth Syst. Sci.*, 25(4):  
892 1689-1709. DOI:10.5194/hess-25-1689-2021

893 Xia, C.-A., Pasetto, D., Hu, B.X., Putti, M., Guadagnini, A., 2020. Integration of  
894 moment equations in a reduced-order modeling strategy for Monte Carlo  
895 simulations of groundwater flow. *J. Hydrol.*, 590: 125257.  
896 DOI:<https://doi.org/10.1016/j.jhydrol.2020.125257>

897 Xia, C.-A., Guadagnini, A., Hu, B. X., Riva, M., Ackerer, P., 2019. Grid convergence

898 for numerical solutions of stochastic moment equations of groundwater flow,  
899 Stoch. Environ. Res. Risk Assess., 33 (8-9), 1565-1579,  
900 <https://doi.org/10.1007/s00477-019-01719-6>.

901 Xia, C.-A., Hu, B.X., Tong, J., Guadagnini, A., 2018. Data Assimilation in  
902 Density-Dependent Subsurface Flows via Localized Iterative Ensemble Kalman  
903 Filter. *Water Resour. Res.*, 54(9): 6259-6281. DOI:10.1029/2017wr022369

904 Xia, C.-A., Li, J., Riva, M., et al., 2024. Characterization of conductivity fields  
905 through iterative ensemble smoother and improved correlation-based adaptive  
906 localization. *J. Hydrol.*, 634: 131054.

907 Xia, C.-A., Wang, H., Jian, W., et al., 2025. Reduced-order Monte Carlo simulation  
908 framework for groundwater flow in randomly heterogeneous composite  
909 transmissivity fields. *J. Hydrol.*, 651: 132593.

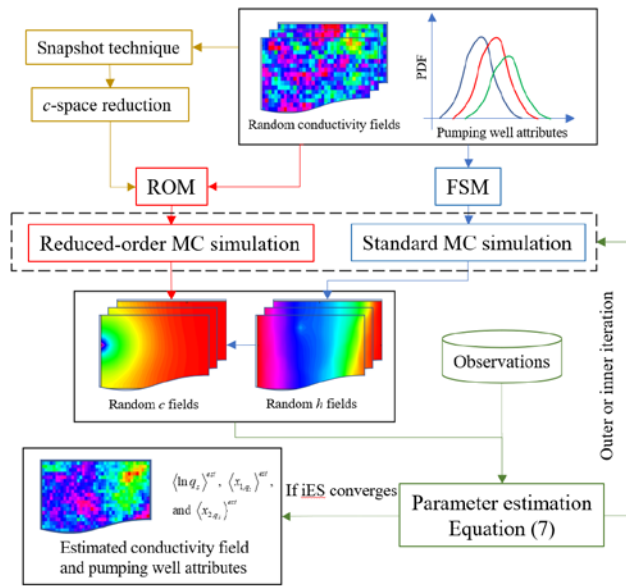
910 Xu, T., Jaime Gomez-Hernandez, J., 2018. Simultaneous identification of a  
911 contaminant source and hydraulic conductivity via the restart normal-score  
912 ensemble Kalman filter. *Adv. Water Resour.*, 112: 106-123.  
913 DOI:10.1016/j.advwatres.2017.12.011

914 Zhang, D., 2002. *Stochastic Method for Flow in Porous Media – Coping with*  
915 *Uncertainties*. Academic Press, Sand Diego, California.

916 Zhang J, Lin G, Li W, et al. An Iterative Local Updating Ensemble Smoother for  
917 Estimation and Uncertainty Assessment of Hydrologic Model Parameters With  
918 Multimodal Distributions. *Water Resour Res*, 2018, 54(3): 1716-33.

919  
 920  
 921  
 922  
 923  
 924

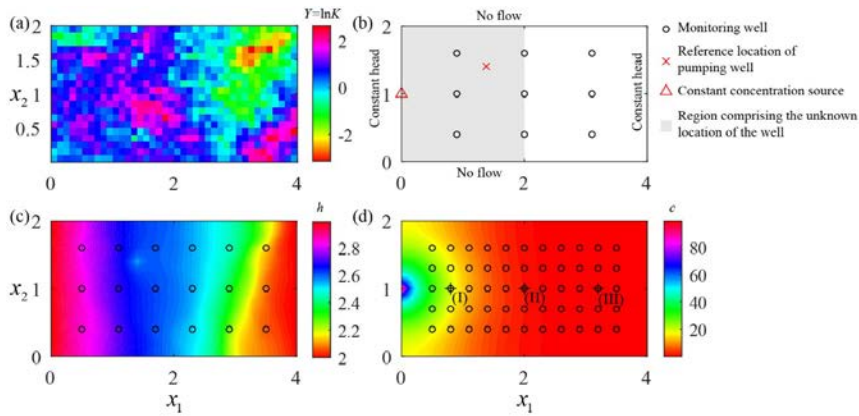
Figures



925

926 Fig. 1 Workflow of iES\_ROM, comprising (i) standard MC simulation of  
 927 groundwater flow (relying on FSM), (ii) reduced-order MC approach for solute  
 928 transport (relying on ROM), and (iii) iES coupled with ROM.

929

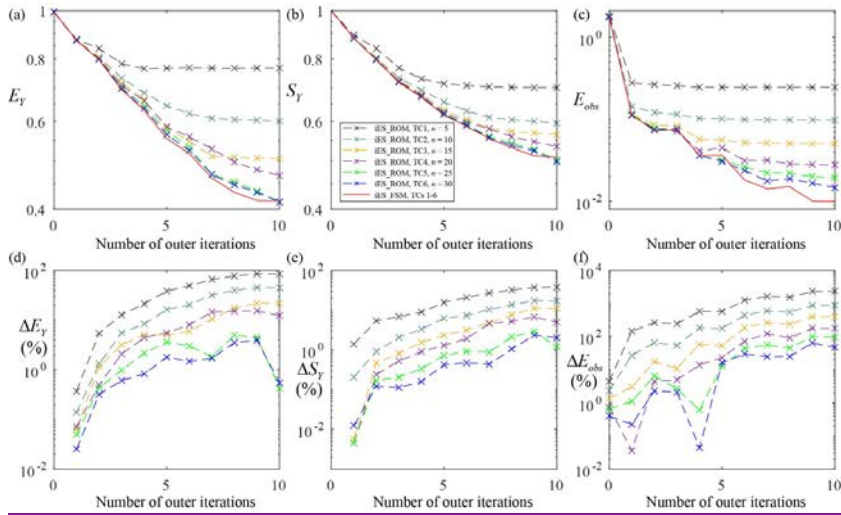


930

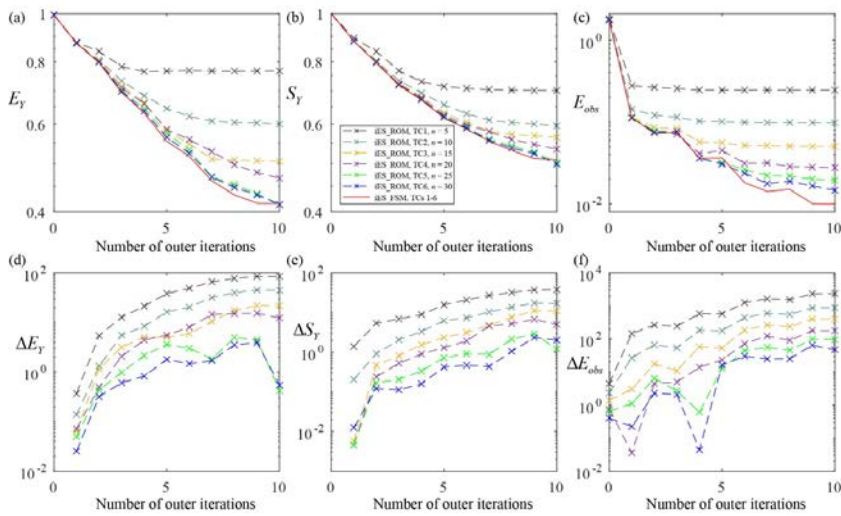
931 Fig. 2 (a) Reference field of  $Y = \ln K$ ; (b) boundary conditions for groundwater flow  
932 and solute transport together with spatial distribution of 9 monitoring wells and  
933 reference location for the pumping well (shaded gray area corresponds to the region  
934 comprising the unknown location of the well); (c) hydraulic head corresponding to the  
935 reference  $Y$  field; and (d) solute concentration corresponding the reference  $Y$  field at  
936 final time step, including three selected locations (i.e., I, II, and III) at which empirical  
937 probability density functions of solute concentration is computed and considered for  
938 illustration purposes. Circles in (b), (c) and (d) correspond to the location of the 9, 18  
939 and 55 monitoring wells, respectively, employed in the study (see Section 3 and Table  
940 1).

941

942



943

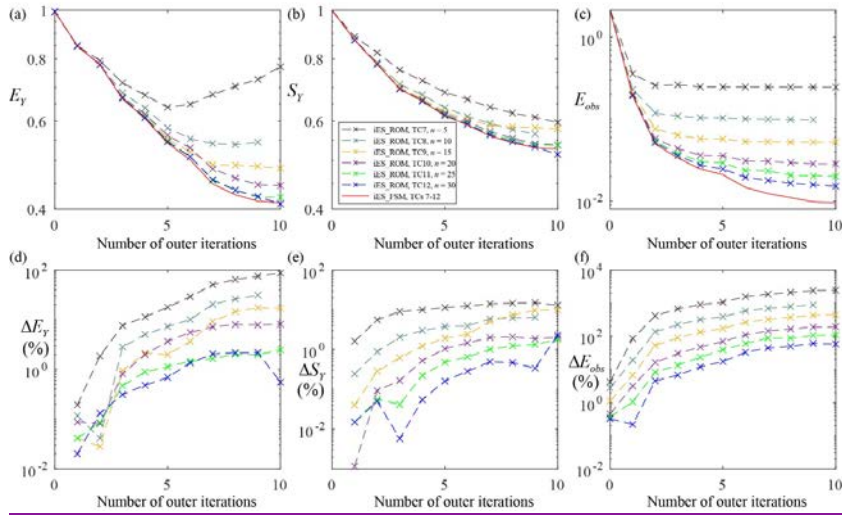


944

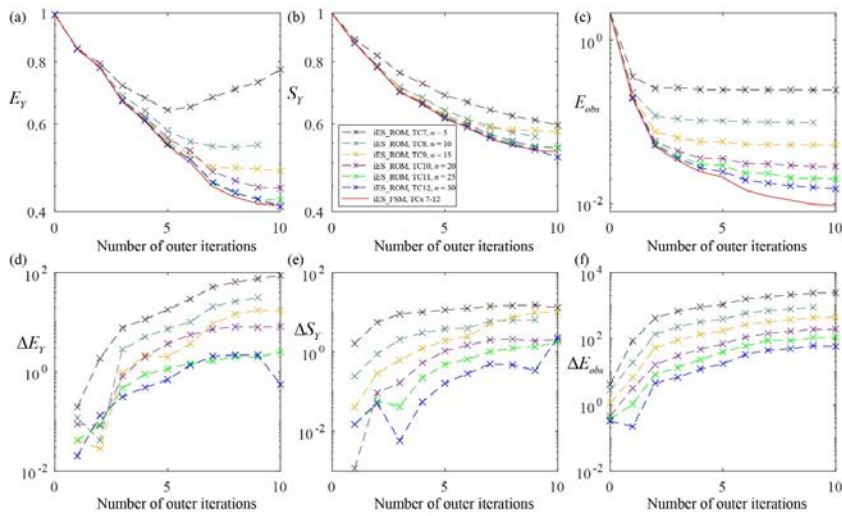
945 Fig. 3 Values of (a)  $E_Y$ , (b)  $S_Y$ , and (c)  $E_{obs}$  versus the number of outer iterations  
 946 obtained through iES\_ROM considering various dimensions of reduced-order model  
 947 (with  $n = 5, 10, 15, 20, 25,$  and  $30$  for TCs 1-6, respectively) and iES\_FSM (which  
 948 provides identical results for TCs 1-6) for ensemble size  $N_{MC} = 10,000$ ;  
 949 corresponding percentage differences between the values of (d)  $E_Y$  ( $\Delta E_Y$ ), (e)  $S_Y$

950  $(\Delta S_Y)$ , and (f)  $E_{obs}$  ( $\Delta E_{obs}$ ) evaluated through iES\_ROM and iES\_FSM.

951



952



953

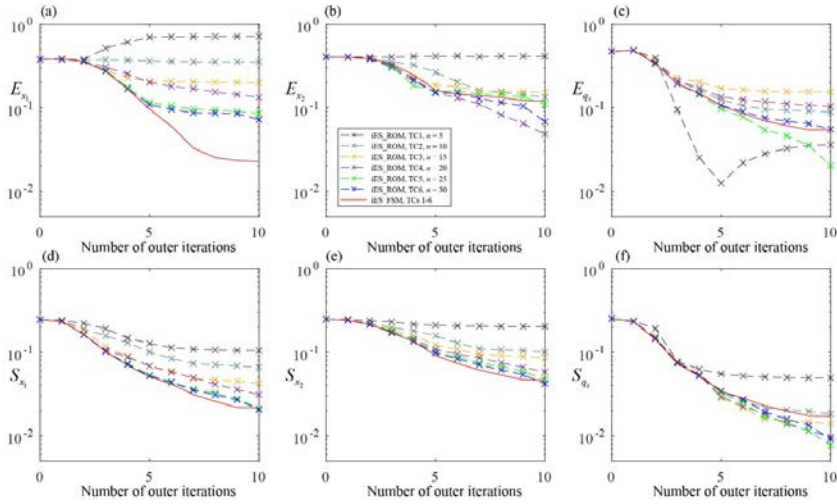
954 Fig. 4 Values of (a)  $E_Y$ , (b)  $S_Y$ , and (c)  $E_{obs}$  versus the number of outer iterations

955 obtained through iES\_ROM considering various dimensions of reduced-order model  
 956 (with  $n = 5, 10, 15, 20, 25$ , and  $30$  for TCs 7-12, respectively) and iES\_FSM (which  
 957 provides identical results for TCs 7-12), when the pumping rate and location are  
 958 previously known and for an ensemble size  $N_{MC} = 10,000$ ; corresponding percentage  
 959 differences between the values of (d)  $E_Y$  ( $\Delta E_Y$ ), (e)  $S_Y$  ( $\Delta S_Y$ ), and (f)  $E_{obs}$

960 ( $\Delta E_{obs}$ ) evaluated through iES\_ROM and iES\_FSM.

961

962

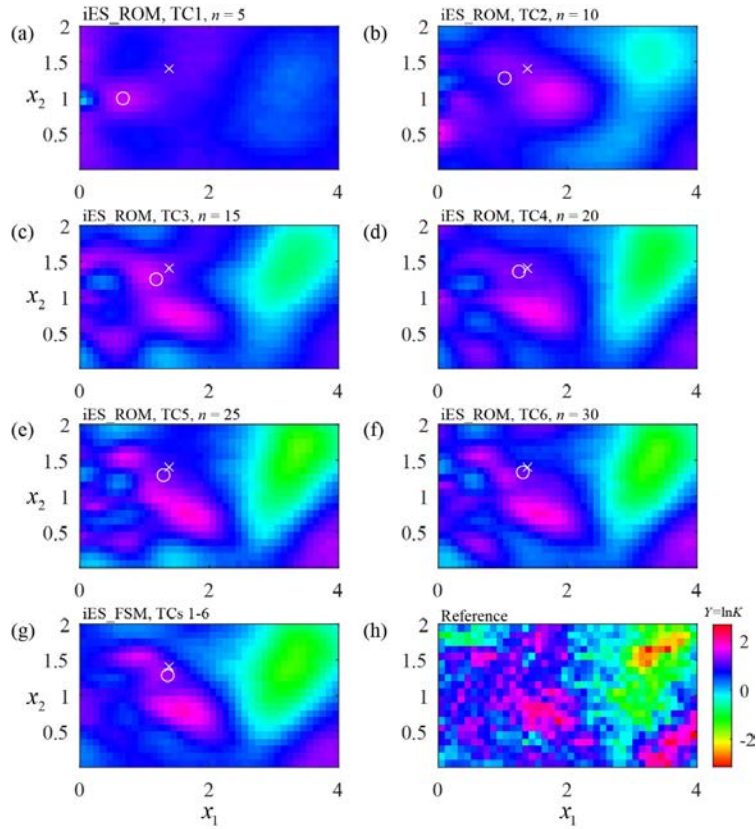


963

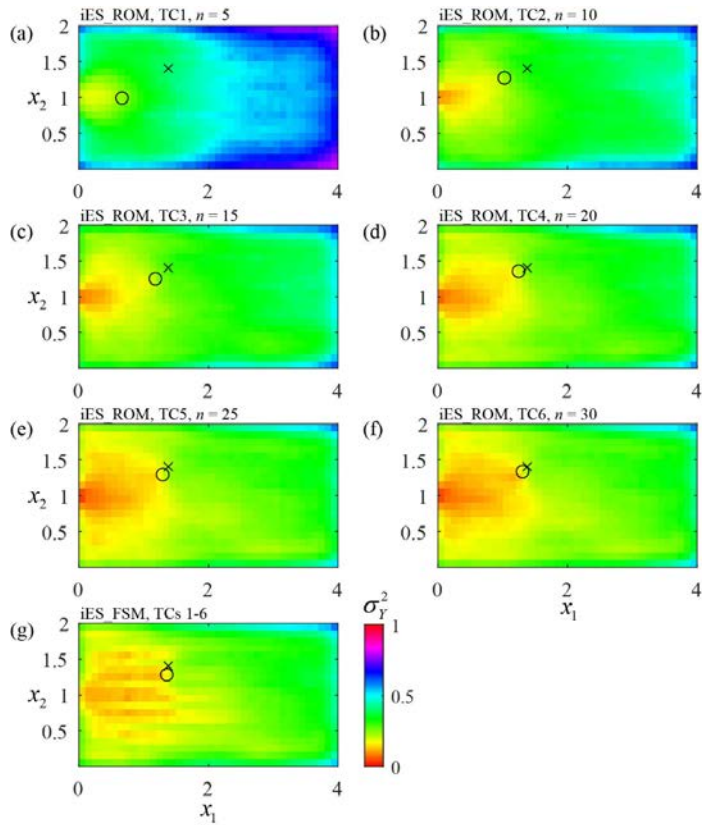
964 Fig. 5 Values of (a)  $E_{x_1}$ , (b)  $E_{x_2}$ , (c)  $E_{q_1}$ , (d)  $S_{x_1}$ , (e)  $S_{x_2}$ , and (f)  $S_{q_1}$  versus the

965 number of outer iterations obtained through iES\_ROM considering various  
 966 dimensions of reduced-order model (with  $n = 5, 10, 15, 20, 25,$  and  $30$  for TCs 1-6,  
 967 respectively) and iES\_FSM (which provides identical results for TCs 1-6), when  $N_{MC}$   
 968  $= 10,000$ .

969



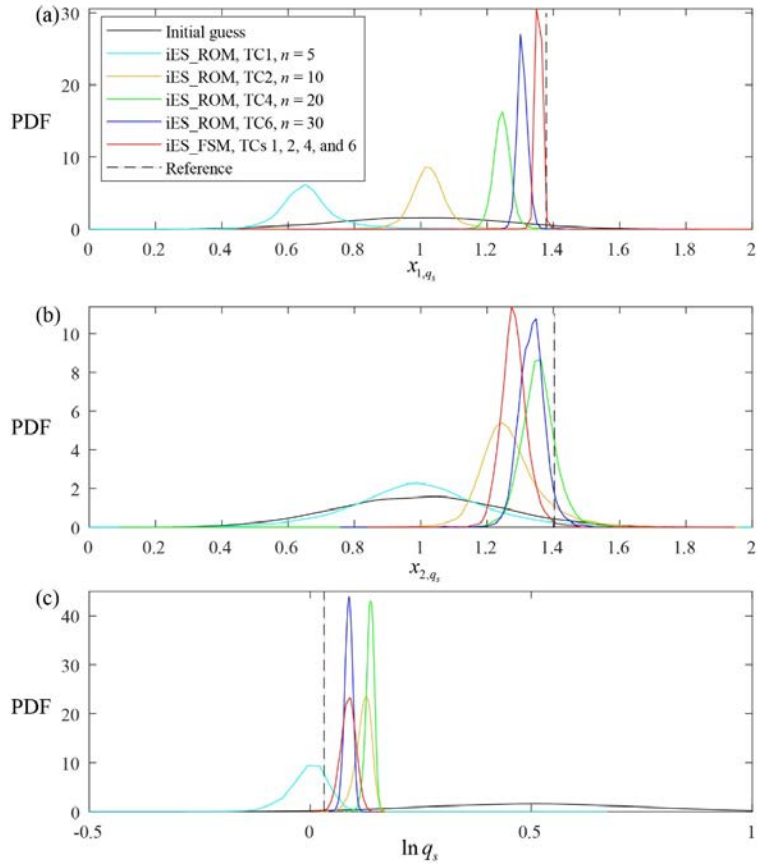
970  
 971 Fig. 6 Estimated (ensemble) mean  $Y$  fields at the final outer iteration through  
 972 iES\_ROM considering different  $n$  (equal to (a) 5, (b) 10, (c) 15, (d) 20, (e) 25, and (f)  
 973 30 for TCs 1-6, respectively) and (g) iES\_FSM (which provides identical results for  
 974 TCs 1-6) when  $N_{MC} = 10,000$ ; (h) reference  $Y$  field.  
 975



977

978 Fig. 7 Estimated (ensemble)  $Y$  variance fields at the final outer iteration through  
 979 iES\_ROM considering different  $n$  (equal to (a) 5, (b) 10, (c) 15, (d) 20, (e) 25, and (f)  
 980 30 for TCs 1-6, respectively) and (g) iES\_FSM (which provides identical results for  
 981 TCs 1-6), when  $N_{MC} = 10,000$ .

982

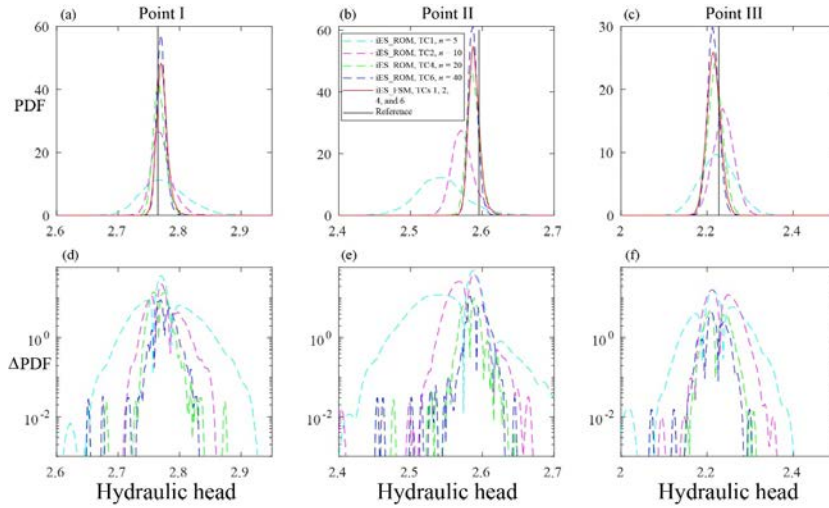


983

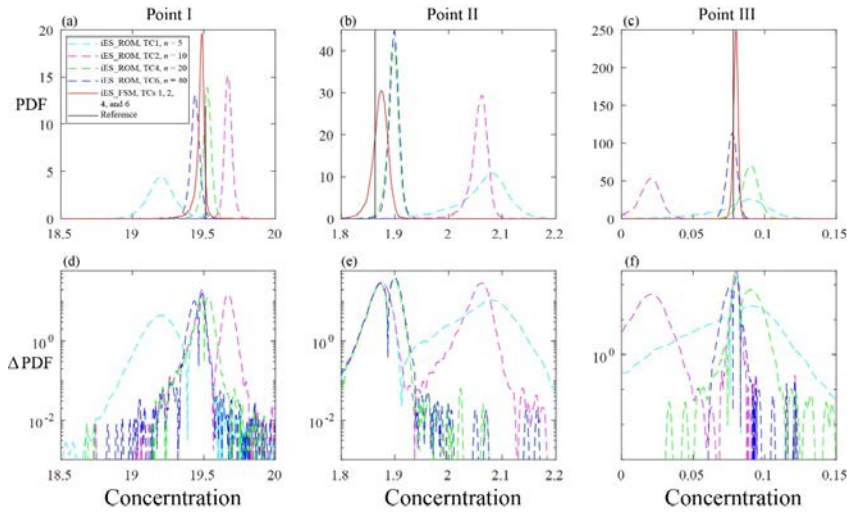
984 Fig. 8 Empirical PDFs of (a)  $x_{1,q_s}$ , (b)  $x_{2,q_s}$ , and (c)  $\ln q_s$  at the final outer iteration

985 through iES\_ROM considering various values of  $n$  (equal to 5, 10, 20, and 30 for TCs  
 986 1, 2, 4, and 6, respectively) and iES\_FSM (which provides identical results for TCs 1,  
 987 2, 4, and 6) when  $N_{MC} = 10,000$ ; corresponding reference values are indicated by  
 988 black dashed lines.

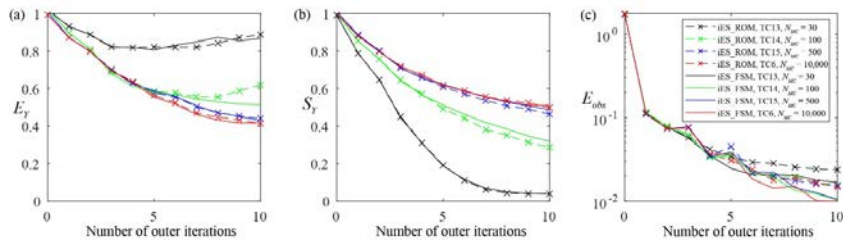
989



990  
 991 Fig. 9 Empirical PDFs of hydraulic head at points (a) I, (b) II, and (c) III (see Fig. 2)  
 992 at the final outer iteration obtained through iES\_ROM considering different values of  
 993  $n$  (equal to 5 (cyan dashed curve), 10 (magenta), 20 (green), and 30 (blue) for TCs 1,  
 994 2, 4, and 6, respectively) and iES\_FSM (red solid curve; identical results for TCs 1, 2,  
 995 4, and 6) when  $N_{MC} = 10,000$  (corresponding reference values are indicated by black  
 996 vertical lines); logarithmic absolute difference between PDFs obtained through  
 997 iES\_ROM and iES\_FSM at points (a) I, (b) II, and (c) III.  
 998



1000  
 1001 Fig. 10 Empirical PDFs of solute concentration at points (a) I, (b) II, and (c) III (see  
 1002 Fig. 2) at the final outer iteration obtained through iES\_ROM considering various  
 1003 values of  $n$  (equal to 5 (cyan dashed curve), 10 (magenta), 20 (green), and 30 (blue))  
 1004 for TCs 1, 2, 4, and 6, respectively) and iES\_FSM (red solid curve; results coincide  
 1005 for TCs 1, 2, 4, and 6) when  $N_{MC} = 10,000$  (corresponding reference values are  
 1006 indicated by black lines); logarithmic absolute difference between PDFs obtained  
 1007 through iES\_ROM and iES\_FSM at points (a) I, (b) II, and (c) III.  
 1008



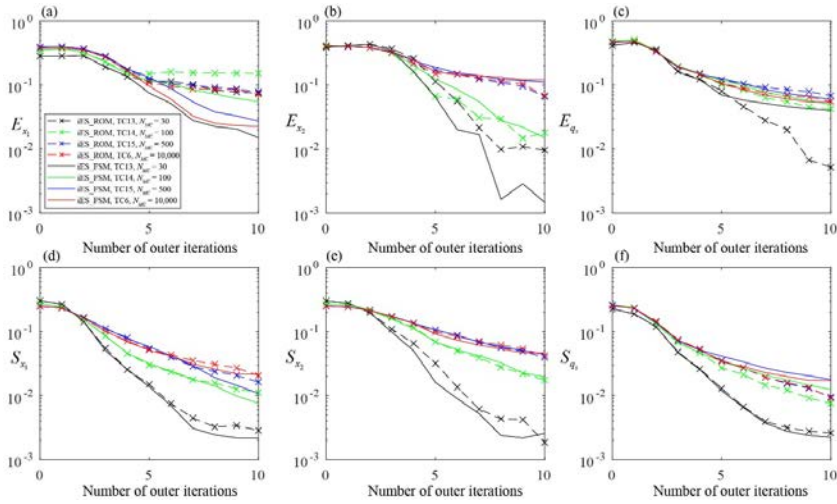
1009

1010 Fig. 11 Values of (a)  $E_Y$ , (b)  $S_Y$ , and (c)  $E_{obs}$  versus the number of outer iterations

1011 obtained through iES\_ROM with  $n = 30$  and iES\_FSM considering various values of

1012  $N_{MC}$  (equal to 30, 100, 500, and 10,000 for TCs 13-15 and 6, respectively).

1013



1014

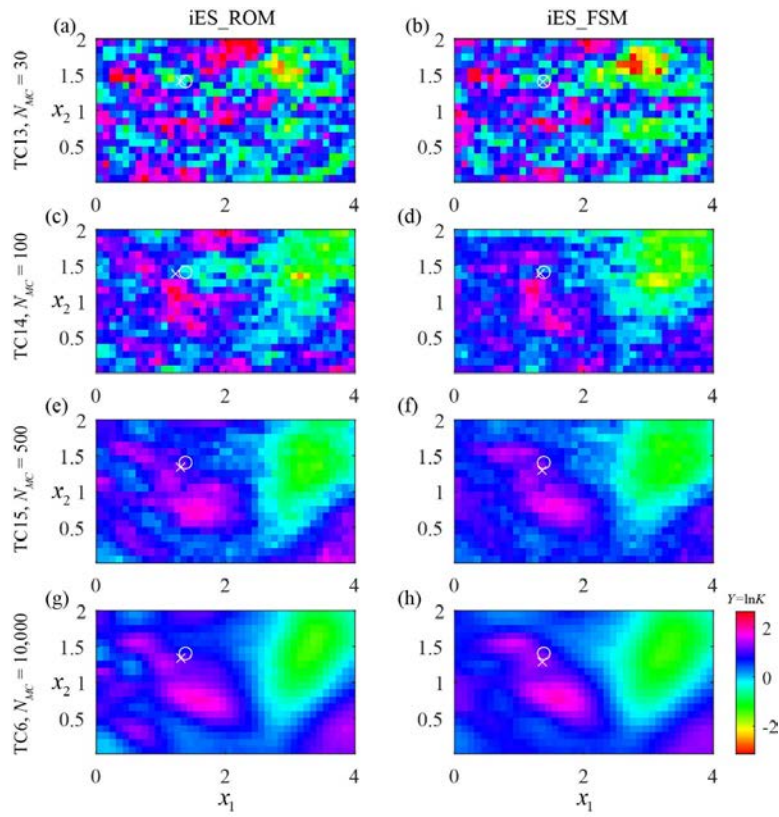
1015 Fig. 12 Values of (a)  $E_{x_1}$ , (b)  $E_{x_2}$ , (c)  $E_{q_s}$ , (d)  $S_{x_1}$ , (e)  $S_{x_2}$ , and (f)  $S_{q_s}$  versus the

1016 number of outer iterations obtained through iES\_ROM with  $n = 30$  and iES\_FSM

1017 considering various values of  $N_{MC}$  (equal to 30, 100, 500, and 10,000 for TCs 13-15

1018 and 6, respectively).

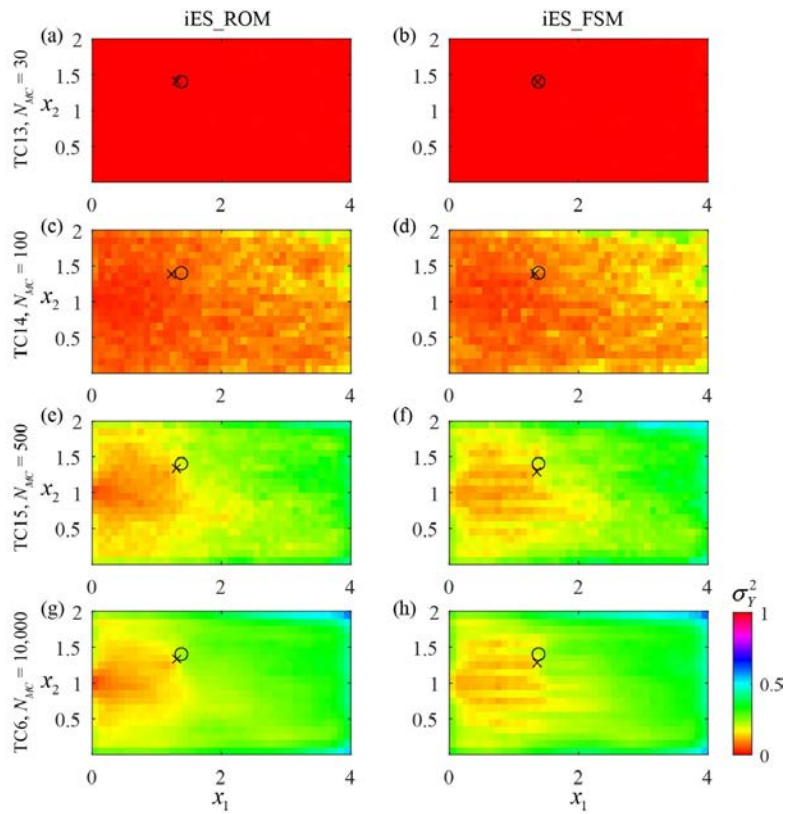
1019



1020

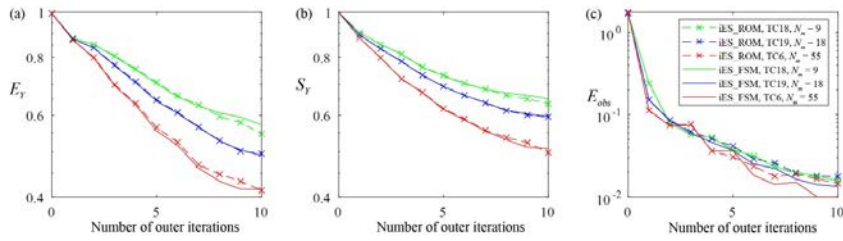
1021 Fig. 13 Estimated (ensemble) mean  $Y$  fields at the final outer iteration obtained  
 1022 through iES\_ROM with  $n = 30$  (left column) and iES\_FSM (right), considering  $N_{MC} =$   
 1023 30 (first row), 100 (second), 500 (third), and 10,000 (bottom) for TCs 13-15 and 6,  
 1024 respectively).

1025



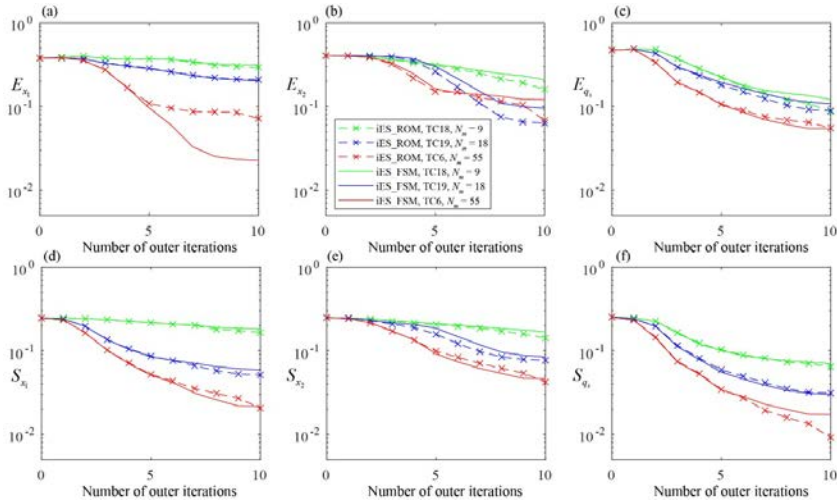
1026

1027 Fig. 14 Estimated (ensemble)  $Y$  variance fields at the final outer iteration obtained  
 1028 through iES\_ROM with  $n = 30$  (left column) and iES\_FSM (right), considering  $N_{MC} =$   
 1029 30 (first row), 100 (second), 500 (third), and 10,000 (bottom) (corresponding to TCs  
 1030 13-15 and 6, respectively).  
 1031



1032

1033 Fig. 15 Values of (a)  $E_Y$ , (b)  $S_Y$ , and (c)  $E_{obs}$  versus the number of outer iterations  
 1034 obtained through iES\_ROM with  $n = 30$  and iES\_FSM considering  $N_m = 9, 18,$  and  $55$   
 1035 (corresponding to TCs 18, 19, and 6, respectively)  
 1036  
 1037



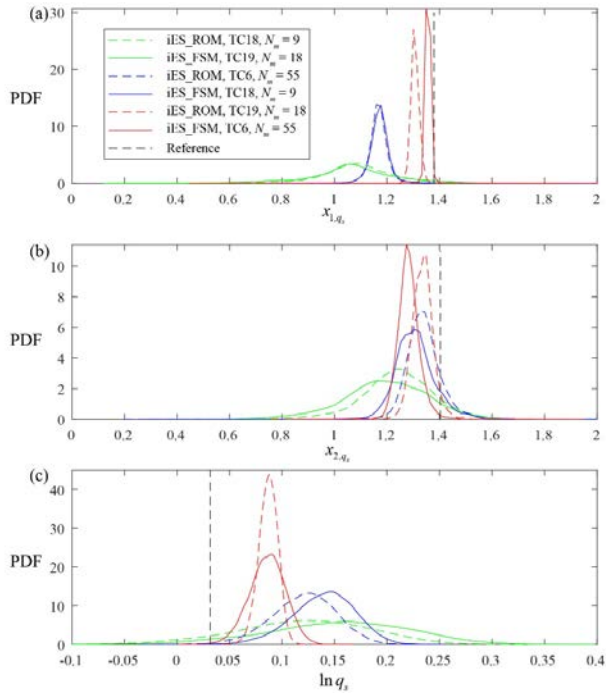
1038

1039 Fig. 16 Values of (a)  $E_{x_1}$ , (b)  $E_{x_2}$ , (c)  $E_{q_s}$ , (d)  $S_{x_1}$ , (e)  $S_{x_2}$ , and (f)  $S_{q_s}$  versus the

1040 number of outer iterations obtained through iES\_ROM with  $n = 30$  and iES\_FSM,

1041 considering  $N_m = 9, 18,$  and  $55$  (corresponding to TCs 18, 19, and 6, respectively).

1042



1043

1044 Fig. 17 Empirical PDFs of (a)  $x_{1,q_s}$ , (b)  $x_{2,q_s}$ , and (c)  $\ln q_s$  at the final outer  
 1045 iteration through iES\_ROM with  $n = 30$  and iES\_FSM (corresponding reference  
 1046 values indicated by black dashed lines) considering  $N_m = 9, 18,$  and  $55$  (corresponding  
 1047 to TCs 18, 19, and 6, respectively).

1048

1049

Tables

1050 Table 1 Overview of the key settings of the test cases (TCs) analyzed. All TCs are

1051 characterized by a zero mean and unit variance of the  $Y$  reference field;  $\mu$  and  $\sigma_Y^2$

1052 denote the mean and variance of the initial ensemble of the  $Y$  fields, respectively.

Group A	Test Case	TC1, TC7	TC2, TC8	TC3, TC9	TC4, TC10	TC5, TC11	TC6, TC12
	$n$	5	10	15	20	25	30
	Known $q_s(\mathbf{x})$ or not	No, Yes	No, Yes	No, Yes	No, Yes	No, Yes	No, Yes
	Approach	iES_FSM and iES_ROM					
Group B	Test Case	TC13	TC14	TC15	TC6		
	$N_{MC}$	30	100	500	10,000		
	Approach	iES_FSM and iES_ROM					
Group C	Test Case	TC16	TC17	TC18	TC19	TC6	
	$\sigma_{obs}$	0.001	0.1	0.01	0.01	0.01	
	$N_m$	55	55	9	18	55	
	Approach	iES_FSM and iES_ROM					
Group D	Test Case	TC20	TC21	TC22	TC23	TC6	
	$\mu$	-0.5	1.5	0.5	0.5	0.5	
	$\sigma_Y^2$	1.0	1.0	0.01	2.0	1.0	
	Approach	iES_FSM and iES_ROM					

	Test Case	TC24	TC25	TC26	TC27	TC28	TC6
Group E	$N_{sn}$	30	100	300	500	1,000	10,000
	Approach	iES_ROM					

1053

1054

1055 Table 2 Values of  $E_Y$ ,  $S_Y$ ,  $E_{obs}$ ,  $E_{x_1}$ ,  $E_{x_2}$ ,  $E_{q_s}$ ,  $S_{x_1}$ ,  $S_{x_2}$ , and  $S_{q_s}$  at the end of  
 1056 the iteration procedure for TC16, TC6, and TC17 obtained through iES\_ROM and  
 1057 iES\_FSM.

	TC16	TC6	TC17	TC16	TC6	TC17	TC16	TC6	TC17
	$E_Y$			$S_Y$			$E_{obs}$		
iES_ROM	0.41	0.41	0.53	0.50	0.50	0.62	0.01	0.02	0.07
iES_FSM	0.41	0.42	0.52	0.51	0.51	0.60	0.01	0.01	0.07
	$E_{x_1}$			$E_{x_2}$			$E_{q_s}$		
iES_ROM	0.07	0.07	0.15	0.08	0.07	0.04	0.05	0.06	0.13
iES_FSM	0.02	0.02	0.06	0.13	0.12	0.09	0.05	0.05	0.11
	$S_{x_1}$			$S_{x_2}$			$S_{q_s}$		
iES_ROM	0.02	0.02	0.04	0.04	0.04	0.08	0.01	0.01	0.03
iES_FSM	0.02	0.02	0.04	0.05	0.05	0.07	0.02	0.02	0.03

1058

1059 Table 3 Values of  $E_Y$ ,  $S_Y$ ,  $E_{obs}$ ,  $E_{x_1}$ ,  $E_{x_2}$ ,  $E_{q_s}$ ,  $S_{x_1}$ ,  $S_{x_2}$ , and  $S_{q_s}$  at the end of  
 1060 the iteration procedure for TC6, TC20, and TC21 obtained through iES\_ROM and  
 1061 iES\_FSM.

Test Case	TC20	TC6	TC21	TC20	TC6	TC21	TC20	TC6	TC21
	$E_Y$			$S_Y$			$E_{obs}$		
iES_ROM	0.51	0.41	0.50	0.60	0.50	0.52	0.02	0.02	0.03
iES_FSM	0.44	0.42	0.52	0.55	0.51	0.56	0.01	0.01	0.03
	$E_{x_1}$			$E_{x_2}$			$E_{q_s}$		
iES_ROM	0.03	0.07	0.12	0.10	0.07	0.10	0.06	0.06	0.08
iES_FSM	0.01	0.02	0.12	0.10	0.12	0.17	0.05	0.05	0.11
	$S_{x_1}$			$S_{x_2}$			$S_{q_s}$		
iES_ROM	0.05	0.02	0.03	0.08	0.04	0.06	0.03	0.01	0.01
iES_FSM	0.03	0.02	0.04	0.06	0.05	0.06	0.02	0.02	0.02

1062

1063 Table 4 Values of  $E_Y$ ,  $S_Y$ ,  $E_{obs}$ ,  $E_{x_1}$ ,  $E_{x_2}$ ,  $E_{q_s}$ ,  $S_{x_1}$ ,  $S_{x_2}$ , and  $S_{q_s}$  at the end of  
 1064 the iteration procedure for TC6, TC22, and TC23 obtained through iES\_ROM and  
 1065 iES\_FSM.

Test Case	TC22	TC6	TC23	TC22	TC6	TC23	TC22	TC6	TC23
	$E_Y$			$S_Y$			$E_{obs}$		
iES_ROM	0.47	0.41	0.46	0.06	0.50	0.77	0.01	0.02	0.02
iES_FSM	0.43	0.42	0.47	0.06	0.51	0.80	0.01	0.01	0.01
	$E_{x_1}$			$E_{x_2}$			$E_{q_s}$		
iES_ROM	0.07	0.07	0.09	0.15	0.07	0.12	0.02	0.06	0.08
iES_FSM	0.02	0.02	0.05	0.22	0.12	0.17	0.02	0.05	0.08
	$S_{x_1}$			$S_{x_2}$			$S_{q_s}$		
iES_ROM	0.003	0.02	0.05	0.004	0.04	0.09	0.003	0.01	0.02
iES_FSM	0.002	0.02	0.04	0.003	0.05	0.08	0.003	0.02	0.03

1066

1067

1068 Table 5 Percentage differences between the values of the selected metrics (i.e.,  $E_Y$ ,  
1069  $S_Y$ ,  $E_{obs}$ ,  $E_{x_1}$ ,  $E_{x_2}$ ,  $E_{q_s}$ ,  $S_{x_1}$ ,  $S_{x_2}$ , and  $S_{q_s}$ ) at the end of the iteration procedure  
1070 for TCs 24-28 obtained through iES\_ROM (values corresponding to TC6 are taken as  
1071 references).

Test Case	$E_Y$	$S_Y$	$E_{obs}$	$E_{x_1}$	$S_{x_1}$	$E_{x_2}$	$S_{x_2}$	$E_{q_s}$	$S_{q_s}$
TC24	11.88	6.34	21.60	44.17	58.50	25.04	34.75	32.29	55.20
TC25	10.16	3.66	6.76	27.83	35.54	13.24	9.58	25.01	37.58
TC26	7.40	1.97	13.00	22.10	16.89	35.54	11.26	13.06	15.09
TC27	4.58	0.14	2.66	11.42	0.17	22.93	1.22	17.74	3.37
TC28	0.50	0.21	4.18	17.19	1.33	31.33	5.86	14.03	0.07

1072

1073